

Adaptivity and Coarsening in the Variational Quasicontinuum Methodology for Localized Damage

O. Rokoš^{a,*}, R.H.J. Peerlings^b, J. Zeman^a

^a*Department of Mechanics, Faculty of Civil Engineering, Czech Technical University in Prague, Thákurova 7, 166 29 Prague 6, Czech Republic.*

^b*Department of Mechanical Engineering, Eindhoven University of Technology, P.O. Box 513, 5600 MB Eindhoven, The Netherlands.*

Abstract

Lattice networks with dissipative interactions are often employed to analyze materials with discrete micro- or meso-structures, or for a description of heterogeneous materials which can be modelled discretely. They are, however, computationally prohibitive for engineering-scale applications. The (variational) QuasiContinuum (QC) method is a concurrent multiscale approach that reduces their computational cost by fully resolving the (dissipative) lattice network in small regions of interest while coarsening elsewhere. When applied to damageable lattices, moving crack tips can be captured by adaptive mesh refinement schemes, whereas fully-resolved trails in crack wakes can be removed by mesh coarsening. In order to address crack propagation efficiently and accurately, we provide in this contribution an adaptive meshing scheme for the variational QC method. To deal with coarsening, we adopt enrichment functions and the partition of unity concept. For the description of crack geometries, the signed distance function is used. Furthermore, necessary changes in the summation rule are presented. Finally, as our standpoint is variational, we discuss implications of the mesh refinement and coarsening from an energy-consistency point of view. All theoretical considerations are demonstrated using two numerical examples for which the resulting reaction forces, energy evolutions, and crack paths are compared to those of the direct numerical simulations.

Keywords: lattice networks, quasicontinuum method, damage, extended finite element method, adaptivity, multiscale modelling, variational formulation

1. Introduction

The mechanical response of materials with discrete micro- or meso-structures such as 3D-printed structures, woven textiles, paper, or foams can be modelled with dissipative lattice networks, cf. e.g. [Ridruejo et al. \(2010\)](#); [Liu et al. \(2010\)](#); [Kulachenko and Uesaka \(2012\)](#); [Beex et al. \(2013\)](#); [Bosco et al. \(2015a,b\)](#). The main advantage of these models consists in

*Corresponding author.

Email address: rokosondrej@gmail.com (O. Rokoš)

their conceptual simplicity, because lattice springs or beams can be identified as individual fibres or yarns of the underlying structure. Therefore, material parameters such as Young’s or hardening moduli, and constitutive damage or plasticity laws can be determined in a relatively straightforward manner. Furthermore, lattice networks incorporate large deformations and yarn reorientations rather easily compared to phenomenological continuum models, see e.g. [Peng and Cao \(2005\)](#). For heterogeneous cohesive-frictional materials such as concrete, lattice networks are capable of capturing distributed microcracking, the heterogeneity at the microscale, and size effects; applications and further discussions can be found, e.g., in [Schlangen and van Mier \(1992\)](#); [Cusatis et al. \(2006\)](#); [Grassl and Jirásek \(2010\)](#); [Eliáš et al. \(2015\)](#).

The main drawback of lattice structures is their considerable computational cost—which may well be prohibitive for engineering applications, in which the lattice spacing is generally several orders of magnitude smaller than the problem size. Ergo, multiscale, or reduced-order modelling methods are required to tackle realistic applications.

A reduced-order modelling method with a concurrent multiscale character is the QuasiContinuum (QC) method. It was originally designed for conservative atomistic systems at the nano-scale level, see [Tadmor et al. \(1996\)](#) for its initial formulation and [Curtin and Miller \(2003\)](#); [Miller and Tadmor \(2002, 2009\)](#); [Iyer and Gavini \(2011\)](#); [Luskin and Ortner \(2013\)](#) for various extensions. This approach was further generalized to tackle materials at the meso-scale level by introducing dissipation along with internal variables in a virtual-power-based format by [Beex et al. \(2014c,d\)](#) and in a variational format by [Rokoš et al. \(2016a,b\)](#). In its essence, the QC methodology resolves the underlying lattice only in small regions of interest, whereas it coarsens it elsewhere. This results in a considerable reduction of the number of Degrees Of Freedom (DOFs), internal variables, and effort to construct the governing equations.

The problem of interest in this contribution is the combination of the QC method and crack propagation in damageable lattice structures, as depicted in [Fig. 1](#). Because most of the dissipation and fibre reorientation occurs near the crack tip, this region must be fully resolved. To this end, a mesh indicator that follows the evolution of the crack tip needs to be provided. Such an approach typically leaves a trail of the fully resolved region in the wake of the crack if no coarsening is included, cf. [Rokoš et al. \(2016b\)](#). It may be clear that, apart from allowing the crack to open up, these fully resolved regions do not contribute to the overall physics and accuracy. It is therefore desirable to coarsen them. However, this coarsening should take into account the effect which the crack has on the local, coarse-scale kinematics of the problem—i.e. it should allow an arbitrary amount of crack opening without any mechanical resistance.

The aim of this contribution is to provide a refinement *and* coarsening strategy that allows for the removal of nodes in the wake of the crack tip to increase the efficiency of the variational QC method. Because the damage in the crack wake is highly localized, it can be treated as a “discontinuity”, although the system is obviously discrete. It is reasonable, therefore, to introduce techniques known from the Extended Finite Element Method (XFEM), ([Belytschko and Black, 1999](#); [Moës et al., 1999](#)), or Generalized Finite Element Method (GFEM),

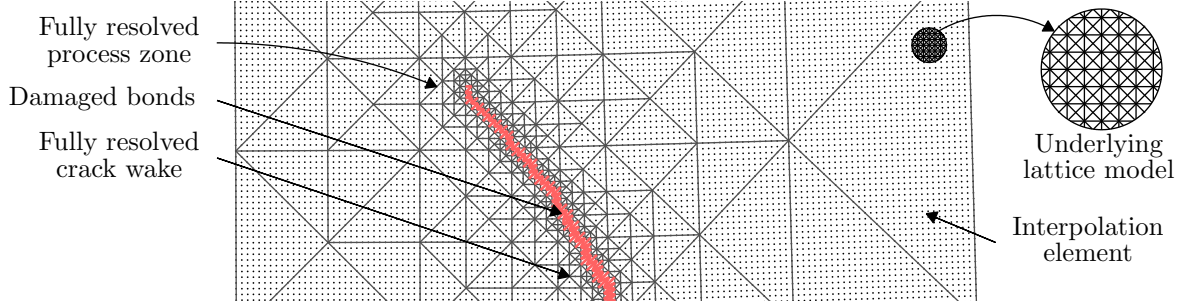


Figure 1: Sketch of a crack propagating in a damageable lattice using an adaptive QC method that only includes mesh refinement. The lattice at the crack tip is fully resolved because large fibre deformations and dissipation occur there. Elsewhere, the displacements are locally homogeneous and no damage occurs, allowing for efficient coarsening and large elements.

(Strouboulis et al., 2000a,b), that rely on the Partition of Unity (PU) concept, (Melenk and Babuška, 1996; Babuška and Melenk, 1997). A certain similarity to the Particle Partition of Unity Method (PPUM), (Griebel and Schweitzer, 2000), can be also observed. Namely, the space of interpolation functions is enriched to also include "jumps" in kinematic as well as in internal variables. As will be explained below, and demonstrated in the examples section, such an enrichment provides an accurate and efficient framework to model cracks in damageable lattices. In what follows, this approach will be referred to as the *eXtended QC* (in analogy to continuum systems), or *X-QC* for short.

Several previous works have focused on adaptivity and coarsening in QC methodologies as well, but these mainly dealt with conservative, atomistic lattice models, cf. Shenoy et al. (1999); Miller and Tadmor (2002); Memarnahavandi et al. (2015). An XFEM-type QC framework was reported in Gracie and Belytschko (2009); Talebi et al. (2013); Aubertin et al. (2009, 2010), which treated atomistic models within the scope of molecular dynamics and the bridging domain method (concurrent coupling between the atomistic and continuum regions). In contrast to these previous works, this contribution focuses on structural lattice networks at the meso-scale level. Moreover, we employ the *dissipative* variational QC with damage, including a *fully non-local* formulation.

The paper is organized as follows. In Section 2, we briefly recall the theory of rate-independent systems on which the variational QC is built. For simplicity, only time-discrete versions of all equations are provided. Having specified the theoretical background, we can introduce the model at hand, its geometry, state variables, and energies driving the evolution. The main developments of this contribution, i.e. the interpolation and summation QC steps revisited from the point of view of lattice structures with localized damage, are discussed in Section 3. Namely, the enrichment functions together with the required changes in the summation rules are introduced in detail. The numerical solution strategy is addressed in Section 4. Two examples demonstrate the additional efficiency of the proposed method. The results show that the coarsening strategy, in particular, allows one to reduce the number of DOFs to approximately 25 – 75 % of that of an adaptive QC without coarsening, with no

significant increase in error. The number of DOFs reduces to 1 – 15 % of that of the Direct Numerical Simulations (DNS). The corresponding computing times are reduced by a factor of 4 – 20, depending on the particular example. The paper closes with a summary and conclusions in Section 6.

2. Variational Formulation of Lattice Networks with Localized Damage

In this section, the basic principles of the variational formulation of rate-independent systems in the context of lattice networks are recalled. For the sake of brevity, we limit ourselves to the time-discrete setting; the general theory is discussed in [Mielke and Roubíček \(2015\)](#), whereas applications to continuous systems can be found, e.g., in [Mühlhaus and Aifantis \(1991\)](#); [Han and Reddy \(1995\)](#); [Bourdin et al. \(2000\)](#); [Mielke et al. \(2002\)](#); [Mielke \(2003\)](#); [Bourdin \(2007\)](#); [Bourdin et al. \(2008\)](#); [Burke et al. \(2010\)](#); [Pham et al. \(2011\)](#); [Hofacker and Miehe \(2012\)](#); [Jirásek and Zeman \(2015\)](#); [Mesgarnejad et al. \(2015\)](#). Applications to lattice networks and QC are presented in [Rokoš et al. \(2016a,b\)](#) for isotropic hardening plasticity and localized damage, respectively.

2.1. General Considerations

An admissible configuration of a rate-independent system of interest is specified by a state variable $\hat{\mathbf{q}} = (\hat{\mathbf{r}}, \hat{\mathbf{z}})$, where $\hat{\mathbf{r}}$ stores the kinematic variables and $\hat{\mathbf{z}}$ the internal variables. All admissible configurations are specified by the state space $\mathcal{Q} = \mathcal{R} \times \mathcal{Z}$, $\hat{\mathbf{r}} \in \mathcal{R}$, $\hat{\mathbf{z}} \in \mathcal{Z}$, which incorporates, e.g., prescribed Dirichlet boundary conditions or constraints on damage variables.

The energetic solution \mathbf{q} is determined using the following incremental minimization problem at time t_k

$$\mathbf{q}(t_k) \in \arg \min_{\hat{\mathbf{q}} \in \mathcal{Q}} \Pi^k(\hat{\mathbf{q}}; \mathbf{q}(t_{k-1})), \quad k = 1, \dots, n_T, \quad (\text{IP})$$

with an initial condition $\mathbf{q}(0) = \mathbf{q}_0$, where $0 = t_0 < t_1 < \dots < t_{n_T} = T$ describes a discrete time horizon $[0, T]$, Π^k denotes an incremental energy of the form

$$\Pi^k(\hat{\mathbf{q}}; \mathbf{q}(t_{k-1})) = \mathcal{E}(t_k, \hat{\mathbf{q}}) + \mathcal{D}(\hat{\mathbf{z}}, \mathbf{z}(t_{k-1})), \quad (\text{IE})$$

and the inclusion sign \in indicates that the potential Π^k is in general nonsmooth or may have multiple minima. The incremental energy consists of the total (Helmholtz type) energy $\mathcal{E} : [0, T] \times \mathcal{Q} \rightarrow \mathbb{R}$, and the dissipation distance $\mathcal{D} : \mathcal{Z} \times \mathcal{Z} \rightarrow \mathbb{R}^+ \cup \{+\infty\}$.

The dissipation distance $\mathcal{D}(\mathbf{z}_2, \mathbf{z}_1)$ measures the minimum dissipation by a continuous transition between two consecutive states \mathbf{z}_1 and \mathbf{z}_2 ; for further details see [Mielke and Roubíček \(2015\)](#), Section 3.2. The potential energy reads

$$\mathcal{E}(t_k, \hat{\mathbf{q}}) = \mathcal{V}(t_k, \hat{\mathbf{q}}) - \mathbf{f}_{\text{ext}}^\top(t_k) \hat{\mathbf{r}}, \quad (1)$$

where $\mathcal{V} : [0, T] \times \mathcal{Q} \rightarrow \mathbb{R}$ is the internally stored energy, $\mathbf{f}_{\text{ext}} : [0, T] \rightarrow \mathcal{R}^*$ represents the column matrix with external loads, and \mathcal{R}^* is the space dual to \mathcal{R} .

Each time the minimization problem (IP) is solved in this contribution, a local minimum that satisfies the energy balance

$$\mathcal{V}(t_k, \mathbf{q}(t_k)) + \text{Var}_{\mathcal{D}}(\mathbf{q}; 0, t_k) = \mathcal{V}(0, \mathbf{q}(0)) + \mathcal{W}_{\text{ext}}(\mathbf{q}; 0, t_k), \quad k = 1, \dots, n_T, \quad (\text{E})$$

is searched. The energy balance (E) equates the internally stored energy plus the *dissipated energy*

$$\text{Var}_{\mathcal{D}}(\mathbf{q}; 0, t_k) = \sum_{l=1}^k \mathcal{D}(\mathbf{z}(t_l), \mathbf{z}(t_{l-1})) \quad (2)$$

with the work performed by the external forces

$$\mathcal{W}_{\text{ext}}(\mathbf{q}; 0, t_k) = \sum_{l=1}^k \frac{1}{2} [\mathbf{f}(t_l) + \mathbf{f}(t_{l-1})]^\top [\mathbf{r}(t_l) - \mathbf{r}(t_{l-1})]. \quad (3)$$

In Eqs. (E), (2), and (3), the symbol $(\mathbf{q}; 0, t_k)$ indicates the dependence on $\mathbf{q}(t_l)$ for $l = 0, \dots, k$.

2.2. Geometry and State Variables

In this section, we briefly specify the geometry, underlying lattice, and the kinematic as well as the internal variables. Our considerations below are limited to 2D lattices for notational simplicity, and lattice nodes are called "atoms".

First, the reader is referred to Fig. 2, where a sketch of the kinematic as well as internal variables is presented. As indicated, we assume an X-braced lattice with the nearest-neighbour interactions. The original location vector of atom α is denoted as $\mathbf{r}_0^\alpha \in \mathbb{R}^2$. For all n_{ato} atoms (collected in an index set N_{ato}), they are stored in the column $\mathbf{r}_0 = [\mathbf{r}_0^1, \dots, \mathbf{r}_0^{n_{\text{ato}}}]^\top$, $\mathbf{r}_0 \in \mathbb{R}^{2n_{\text{ato}}}$. By analogy, the current location vectors $\mathbf{r}^\alpha(t_k) \in \mathbb{R}^2$ are stored in $\mathbf{r}(t_k) = [\mathbf{r}^1(t_k), \dots, \mathbf{r}^{n_{\text{ato}}}(t_k)]^\top$.

The entire system contains n_{int} interactions stored in an index set N_{int} . Each interaction $\alpha\beta \in N_{\text{int}}$ that connects atoms α and β is of the length

$$r^{\alpha\beta}(t_k) = \|\mathbf{r}^\beta(t_k) - \mathbf{r}^\alpha(t_k)\|_2, \quad \alpha\beta = 1, \dots, n_{\text{ato}}, \quad (4)$$

where $\|\bullet\|_2$ denotes the Euclidean norm.

For *damaging* interactions, cf. Fig. 2b, the only internal variable is the damage variable $\omega(t_k) \in [0, 1]$. All of these damage variables are stored in the column $\mathbf{z}(t_k)$, which is hence of length n_{int} .

2.3. Definition of Energies

The internally stored energy associated with damaging lattices reads

$$\mathcal{V}(\hat{\mathbf{r}}, \hat{\mathbf{z}}) = \frac{1}{2} \sum_{\alpha, \beta \in B_\alpha} \left[(1 - \hat{\omega}^{\alpha\beta}) \phi^{\alpha\beta}(\hat{\mathbf{r}}_+^{\alpha\beta}) + \phi^{\alpha\beta}(\hat{\mathbf{r}}_-^{\alpha\beta}) \right], \quad (5)$$

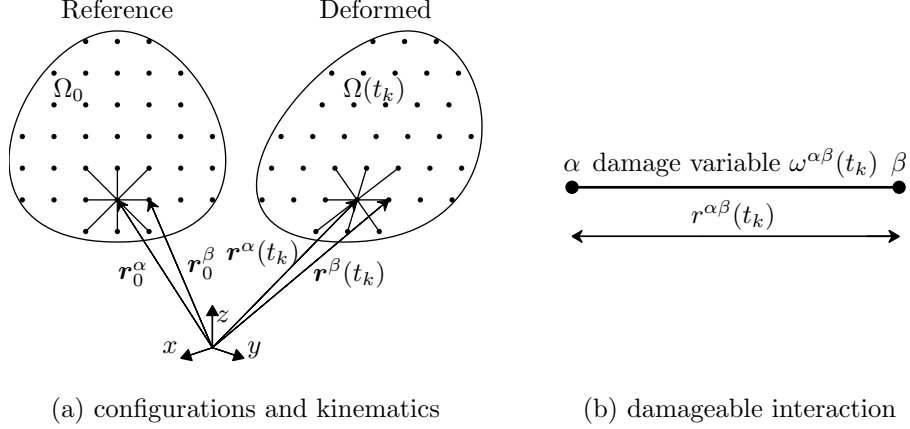


Figure 2: Sketch of system configurations and kinematic as well as internal variables.

where $B_\alpha \subseteq N_{\text{ato}}$ denotes the set of the nearest neighbours associated with atom α . The elastic energy of a bond $\phi^{\alpha\beta}$ is reduced by the damage variable ω only if the bond is loaded in tension to better reflect physical behaviour of damageable materials. In Eq. (5), we have introduced $\hat{r}_+^{\alpha\beta} = \max(\hat{r}^{\alpha\beta}, r_0^{\alpha\beta})$, $\hat{r}_-^{\alpha\beta} = \min(\hat{r}^{\alpha\beta}, r_0^{\alpha\beta})$, and assumed $\phi^{\alpha\beta}(r_0^{\alpha\beta}) = 0$.

The dissipation distance for bond $\alpha\beta$ for two consecutive states $\hat{\mathbf{z}}_1$ and $\hat{\mathbf{z}}_2$ is defined as

$$\mathcal{D}^{\alpha\beta}(\hat{\mathbf{z}}_2, \hat{\mathbf{z}}_1) = \begin{cases} D^{\alpha\beta}(\hat{\omega}_2^{\alpha\beta}) - D^{\alpha\beta}(\hat{\omega}_1^{\alpha\beta}) & \text{if } \hat{\omega}_2^{\alpha\beta} \geq \hat{\omega}_1^{\alpha\beta} \\ +\infty & \text{otherwise,} \end{cases} \quad \alpha\beta \in N_{\text{int}}, \quad (6)$$

and the total dissipation distance is specified as

$$\mathcal{D}(\hat{\mathbf{z}}_2, \hat{\mathbf{z}}_1) = \frac{1}{2} \sum_{\alpha, \beta \in B_\alpha} \mathcal{D}^{\alpha\beta}(\hat{\mathbf{z}}_2, \hat{\mathbf{z}}_1). \quad (7)$$

In definition (6), $D^{\alpha\beta}(\omega^{\alpha\beta})$ is the energy dissipation of a single bond during a unidirectional damage process up to a damage level $\omega^{\alpha\beta}$. This function therefore increases from $D^{\alpha\beta}(0) = 0$ to $D^{\alpha\beta}(1) = g_{f,\infty}$, where $g_{f,\infty}$ is the energy dissipated at complete failure.

The incremental interaction energy, $\tilde{\pi}_{\alpha\beta}^k$, and incremental site energy, π_α^k , then read:

$$\tilde{\pi}_{\alpha\beta}^k(\hat{\mathbf{q}}; \mathbf{q}(t_{k-1})) = (1 - \hat{\omega}^{\alpha\beta})\phi^{\alpha\beta}(\hat{r}_+^{\alpha\beta}) + \phi^{\alpha\beta}(\hat{r}_-^{\alpha\beta}) + \mathcal{D}^{\alpha\beta}(\hat{\omega}^{\alpha\beta}, \omega^{\alpha\beta}(t_{k-1})), \quad \alpha\beta = 1, \dots, n_{\text{int}}, \quad (8a)$$

$$\pi_\alpha^k(\hat{\mathbf{q}}; \mathbf{q}(t_{k-1})) = \frac{1}{2} \sum_{\beta \in B_\alpha} \tilde{\pi}_{\alpha\beta}^k(\hat{\mathbf{q}}, \mathbf{q}(t_{k-1})), \quad \alpha = 1, \dots, n_{\text{ato}}. \quad (8b)$$

3. Variational Quasicontinuum Methodology with Refinement and Coarsening

In this section we specify the two steps of the standard QC methodology, interpolation and summation, as well as additional procedures that must be adopted to extend it to an

efficient description for localized damage. We start with a geometric crack description for lattice systems in Section 3.1, proceeding to the interpolation step in Section 3.2, where the standard framework as well as the mesh refinement and the mesh coarsening are treated. The first part closes with the description of the enrichment functions. The second part is devoted to summation, starting with the standard framework in Section 3.3, which is later extended to incorporate also the enrichment functions. Finally, the complete X-QC procedure is summarized in Section 3.4 in terms of a general algorithm, and energy implications are discussed in Section 3.5 in order to allow for proper verification of the energy equality (E).

3.1. Description of a Crack

In what follows, a crack is defined as an ordered set of points collected in a set C , cf. also Fries and Baydoun (2012):

$$\text{If } \omega^{\alpha\beta} \geq \eta \quad \text{then} \quad \frac{1}{2}(\mathbf{r}_0^\alpha + \mathbf{r}_0^\beta) \in C, \quad \text{and} \quad \alpha, \beta \in N_{\text{cw}}. \quad (9)$$

The set N_{cw} collects all crack wake atoms, whereas C stores the midpoints of all fully damaged bonds. Upon ordering, the set C defines an oriented polygon $\Gamma_C(s)$ (a curve parametrized by a curvilinear coordinate s) geometrically representing the crack. The threshold $\eta \in (0, 1)$ should be close enough to 1, e.g. $\eta = 0.95$. Naturally, any duplicates in (9) are eliminated, and the ordering may be implemented in various ways, e.g. by sorting the points in C with respect to their x -coordinates.¹

For future use, it is convenient to introduce the signed distance function ψ , cf. e.g. Fries and Belytschko (2010), Section 3. Its definition reads

$$\begin{aligned} \mathbf{c}^\alpha &= \arg \min_{\hat{\mathbf{c}} \in \Gamma_C} \|\mathbf{r}_0^\alpha - \hat{\mathbf{c}}\|, \\ \psi(\mathbf{r}_0^\alpha) &= \|\mathbf{r}_0^\alpha - \mathbf{c}^\alpha\| \cdot \text{sign}(\mathbf{n}_{\mathbf{c}^\alpha}^\top (\mathbf{r}_0^\alpha - \mathbf{c}^\alpha)), \end{aligned} \quad \alpha \in N_{\text{ato}}, \quad (10)$$

where $\mathbf{n}_{\mathbf{c}^\alpha}$ denotes the column storing the unit normal to the crack Γ_C at the closest point \mathbf{c}^α . For instance, $\mathbf{n}_{\mathbf{c}^\alpha}$ can be defined such that $\mathbf{t}_{\mathbf{c}^\alpha} \times \mathbf{n}_{\mathbf{c}^\alpha} = \mathbf{e}_z$, where $\mathbf{t}_{\mathbf{c}^\alpha}$ is the tangent vector to Γ_C at \mathbf{c}^α , and \mathbf{e}_z is the unit basis vector pointing in the z -direction of the adopted coordinate system. If \mathbf{c}^α is situated at a kink of Γ_C , entire cone of normals must be considered; then, the sign of $\psi(\mathbf{r}_0^\alpha)$ is positive if the vector $\mathbf{r}_0^\alpha - \mathbf{c}^\alpha$ belongs to the cone of normals and negative otherwise. The function ψ is therefore positive on one side of the crack and negative on the other. Because the crack tip is always located inside the fully refined region, no second level set function is required to describe the crack tip, cf. Fries and Belytschko (2010), Section 3.2. For a pictorial representation of the introduced quantities see Fig. 3.

3.2. Interpolation

In the four following subsections, the interpolation step of the QC method and its effect on the incremental energy of the full system (Π^k in (IE)) are detailed.

¹Note that in the case of extensive distributed cracking, definition (9) may not be sufficient and the X-QC presented here cannot be employed. In those cases, it is reasonable to fully resolve such regions.

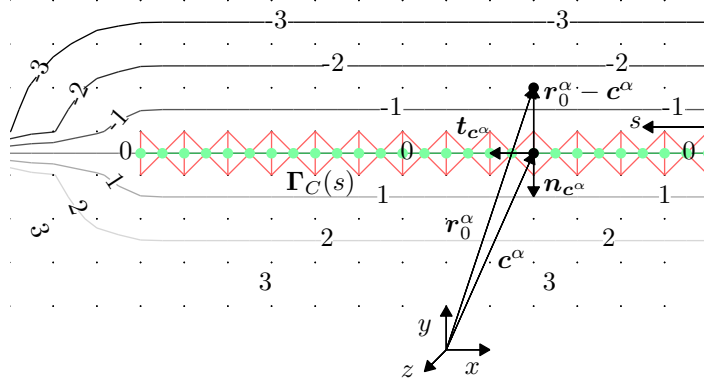


Figure 3: Representation of an existing crack in a discrete lattice network. Damaged bonds (for which $\omega^{\alpha\beta} \geq \eta$, cf. definition (9)) are depicted by red lines (other interactions are omitted for clarity) and set C is depicted using green dots. The signed distance function ψ is represented by contour lines, and the crack polygon Γ_C is presented as a green line. Atom sites are shown as black dots.

3.2.1. General Framework

Interpolation introduces to the minimization problem (IP) the following equality constraints:

$$\hat{\mathbf{r}} = \Phi \hat{\mathbf{g}}, \quad \text{for } \hat{\mathbf{g}} \in \mathcal{G}(t_k), \quad (11)$$

where $\hat{\mathbf{g}}$ denotes a column of generalized DOFs located in a kinematically constrained subspace $\mathcal{G}(t_k)$ of the fully dimensional space $\mathcal{R}(t_k)$.

After substitution of Eq. (11), the incremental energy (IE) becomes a function of $\hat{\mathbf{g}}$, i.e.

$$\Pi^k(\hat{\mathbf{r}}, \hat{\mathbf{z}}; \mathbf{r}(t_{k-1}), \mathbf{z}(t_{k-1})) = \Pi^k(\Phi \hat{\mathbf{g}}, \hat{\mathbf{z}}; \Phi \mathbf{g}(t_{k-1}), \mathbf{z}(t_{k-1})), \quad (12)$$

which can be minimized over the subspace $\mathcal{G}(t_k)$. This reduces the computational effort if $\dim(\mathcal{G}(t_k)) \ll \dim(\mathcal{R}(t_k))$.

In QC approaches, the generalised DOFs $\hat{\mathbf{g}}$ are chosen as the DOFs of a small set of atoms, the so-called *repatoms*. Usually, repatoms are chosen as nodes of a mesh \mathcal{T} that triangulates the domain Ω_0 , and the interpolation is implemented via piecewise affine (P₁) FE shape functions constructed between the repatoms. Consequently, Φ contains standard FEM shape function evaluations at all atom positions, cf. e.g. [Tadmor and Miller \(2011\)](#). Note that higher-order polynomial approximations inside elements can be adopted as well, see e.g. [Beex et al. \(2014a\)](#), [Yang and To \(2015\)](#), or [Beex et al. \(2015b\)](#).

In order to distinguish classical QC approach from its extended version presented below, we use the following notation for the classical QC: all n_{rep} repatoms are collected in an index set $N_{\text{rep}} \subseteq N_{\text{ato}}$, whereas their admissible positions $\hat{\mathbf{r}}_{\text{rep}}^\alpha \in \mathbb{R}^2$, $\alpha \in N_{\text{rep}}$, are stored in the column $\hat{\mathbf{r}}_{\text{rep}} \in \mathcal{R}_{\text{rep}}(t_k)$ by analogy to $\hat{\mathbf{r}}$. Associated interpolation matrix is denoted Φ_{FE} .

3.2.2. Mesh Refinement

In this contribution, the mesh refinement indicator of [Rokoš et al. \(2016b\)](#), is adopted with minor changes. It proceeds as follows: a triangle K of the current triangulation \mathcal{T}_k is endowed with a set of sampling interactions S_{int}^K specified as

$$S_{\text{int}}^K \text{ stores those interactions } \alpha\beta \in S_{\text{int}} \text{ for which } \frac{1}{2}(\mathbf{r}^\alpha + \mathbf{r}^\beta) \in K. \quad (13)$$

Then, the following energy condition is introduced

$$(1 - \omega^{\alpha\beta})\phi^{\alpha\beta}(r_+^{\alpha\beta}) \geq \theta_r \phi_{\text{th}}^{\alpha\beta}, \quad \alpha\beta \in S_{\text{int}}^K, \quad \theta_r \in (0, 1), \quad (14)$$

which specifies interactions that are likely to be damaged. In Eq. (14), $\phi^{\alpha\beta}$ denotes the pair potential, θ_r a refinement safety parameter, and $\phi_{\text{th}}^{\alpha\beta}$ the stored threshold energy at which the internal variable starts to evolve. The mesh refinement indicator then reads

$$\begin{aligned} &\text{If condition (14) holds at least for one interaction } \alpha\beta \in S_{\text{int}}^K \\ &\implies \text{ mark } K \text{ for refinement, i.e. add } K \text{ to } \mathcal{I}_r. \end{aligned} \quad (15)$$

Having specified a set of triangles marked for refinement, $\mathcal{I}_r \subseteq \mathcal{T}_k$, the current triangulation \mathcal{T}_k must be refined. To this end, the backward-logest-edge-bisection algorithm by [Rivara \(1997\)](#) is used.

3.2.3. Mesh Coarsening

Before coarsening the current triangulation \mathcal{T}_k , first an indicator is presented that marks which triangles need to be coarsened. In analogy to Eq. (14) we introduce the following energy condition

$$(1 - \omega^{\alpha\beta})\phi^{\alpha\beta}(r_+^{\alpha\beta}) + \phi^{\alpha\beta}(r_-^{\alpha\beta}) \leq \theta_c \phi_{\text{th}}^{\alpha\beta}, \quad \alpha\beta \in S_{\text{int}}^K, \quad \theta_c \in (0, 1), \quad \theta_c < \theta_r, \quad (16)$$

where the compressive part is now included as well. The rationale behind condition (16) is that in the crack wake the stress is low, and hence also the energy. The mesh coarsening indicator then reads

$$\begin{aligned} &\text{If condition (16) holds for all interactions } \alpha\beta \in S_{\text{int}}^K \\ &\implies \text{ mark } K \text{ for coarsening, i.e. add } K \text{ to } \mathcal{I}_c. \end{aligned} \quad (17)$$

Verifying condition (17) for all elements yields a set of triangles marked for coarsening, $\mathcal{I}_c \subseteq \mathcal{T}_k$.

Note that because the damage remains localized, it yields steep spatial (interaction) energy variations in the vicinity of the crack tip. For instance, in Fig. 4, the normalized interaction energy can be seen to drop from 1.2 to 0.2 over just two to three lattice spacings. From this it may be clear that if the values of θ_c and θ_r are too close, or if θ_c is too high, mesh oscillations may occur in subsequent time steps. In order to achieve good performance,

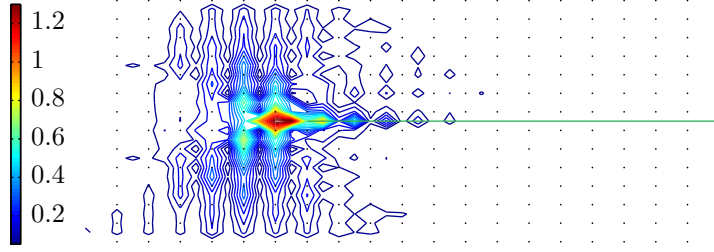


Figure 4: An example of contours of normalized energy $\phi^{\alpha\beta}/\phi_{\text{th}}^{\alpha\beta}$ around a crack tip (based on linearly interpolated data) of a QC system. Regular atom sites are shown as black dots and the existing crack as a green line.

i.e. to avoid mesh oscillations, θ_c should be relatively small compared to θ_r . In particular, we choose $\theta_r = 0.5$ or 0.25 and $\theta_c = 0.05$ in both examples of Section 5.

In order to coarsen the current triangulation \mathcal{T}_k , a similar algorithm to those proposed by [Chen and Zhang \(2010\)](#) and [Funken et al. \(2010\)](#) is adopted. Because we use the two-triangle refinement scheme, the entire binary-tree structure of the triangulation history must be stored. Coarsening of a patch of triangles is decided based on their nodes, cf. Fig. 5. All nodes (repatoms) of the current triangulation are stored in a set N_{rep} , which is divided into three disjoint sets: N_r , N_c , and N_u . The set N_r stores nodes associated with triangles in \mathcal{I}_r (and also other protected nodes, see Alg. 2). The set N_c collects nodes associated with triangles in \mathcal{I}_c , and N_u complements N_{rep} . As a consequence of the mesh hierarchy, only a subset of N_c can be removed. These are identified through their valences v_α (the number of triangles connected to a node):

$$v_\alpha = \#\{K \in \mathcal{T}_k \mid \alpha \in K\}, \quad \alpha \in N_c. \quad (18)$$

Only nodes with valence $v_\alpha = 2$ (boundary nodes) or 4 (internal nodes) can be removed (the blue points in Fig. 5). The corresponding two or four child elements are subsequently replaced with one or two parent elements, shifting locally the binary-tree hierarchy of the mesh one level up. As valences change during the coarsening process, this procedure is repeated until convergence.

In what follows, we use a right-angled initial triangulation \mathcal{T}_0 , as already indicated in Fig. 5. Because the above described refinement and coarsening algorithms yield self-similar triangulations, all meshes \mathcal{T}_k are right-angled as well. This is desirable because the summation error is minimized, cf. [Rokoš et al. \(2016a\)](#), and poorly shaped triangles are avoided.

An alternative approach to the mesh refinement and coarsening indicators, proposed in Eqs. (15) and (17), would be to use *error estimators* such as the *goal-oriented* error estimator reported e.g. in [Becker and Rannacher \(2001\)](#); [Oden and Prudhomme \(2002\)](#); [Prudhomme et al. \(2006\)](#); [Memarnahavandi et al. \(2015\)](#). Generalizations of this type will

²Note that since all elements $K \in \mathcal{T}_k$ are considered as closed sets, bonds lying on edges may belong to two triangles.

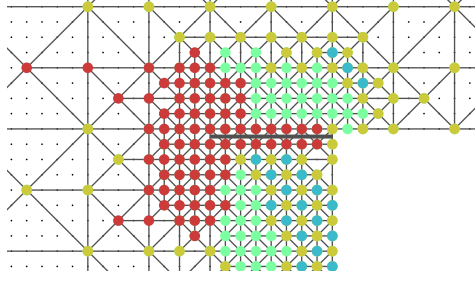


Figure 5: A typical situation before coarsening. The red points define the set N_r . They are found at, and ahead of, the crack tip, and are protected from coarsening. The yellow along with the blue points define the set N_c , and can be coarsened. The green points remain unchanged and correspond to the set N_u . Only the blue points satisfy the valence condition and can be removed. Regular atoms are shown as black dots and the current triangulation \mathcal{T}_k is depicted in black thin lines. The existing crack is indicated as a thick black line. All interactions are omitted for clarity.

not be developed in this contribution and are left as a possible future challenge.

3.2.4. Enrichment Functions

In Sections 3.2.1 – 3.2.3 we discussed the QC interpolation and mesh coarsening independently of an existing crack—the crack served merely to identify the fully resolved region at its tip and a coarse region elsewhere. In this subsection, we describe how to extend the QC interpolation when the current triangulation \mathcal{T}_k is such that a crack cuts through a coarse triangle K , and how it influences Φ , $\hat{\mathbf{r}}_{\text{rep}}$, and $\hat{\mathbf{g}}$. Similarly to the previous sections, the discussion considers the system at time step t_k .

We first specify the cut elements (also called reproducing, [Fries and Belytschko 2010](#)), cf. Fig. 6a. A coarse element $K \in \mathcal{T}_k$ such that

$$\#(C \cap K) > 0 \quad \text{and} \quad \min_{\mathbf{r}_0^\alpha \in K} \psi(\mathbf{r}_0^\alpha) \cdot \max_{\mathbf{r}_0^\alpha \in K} \psi(\mathbf{r}_0^\alpha) < 0 \quad (19)$$

is considered to be cut by a crack. Conditions (19) require that at least one point in C belongs to K and that the signed distance function ψ changes its sign inside K . Let us assume in what follows that a crack cannot cut directly through any of the nodes, atoms, or along domain boundaries.

Assume then that our system is approximated with a standard QC framework in which the positions of the repatoms are collected in a column $\hat{\mathbf{r}}_{\text{rep}}$. Then, the reconstruction in Eq. (11) can be rewritten as

$$\hat{\mathbf{r}}_{\text{qc}}^\alpha = \sum_{\beta \in N_{\text{rep}}} \varphi_\beta(\mathbf{r}_0^\alpha) \hat{\mathbf{r}}_{\text{rep}}^\beta, \quad \alpha \in N_{\text{ato}}, \quad (20)$$

where $\varphi_\beta(\mathbf{r}_0^\alpha)$ represents the P_1 FE shape function associated with the repatom β (this function is evaluated at the undeformed configuration of atom α), and $\hat{\mathbf{r}}_{\text{rep}}^\beta \in \mathbb{R}^2$ denotes an admissible position of a repatom β . This definition does not include an existing crack yet.

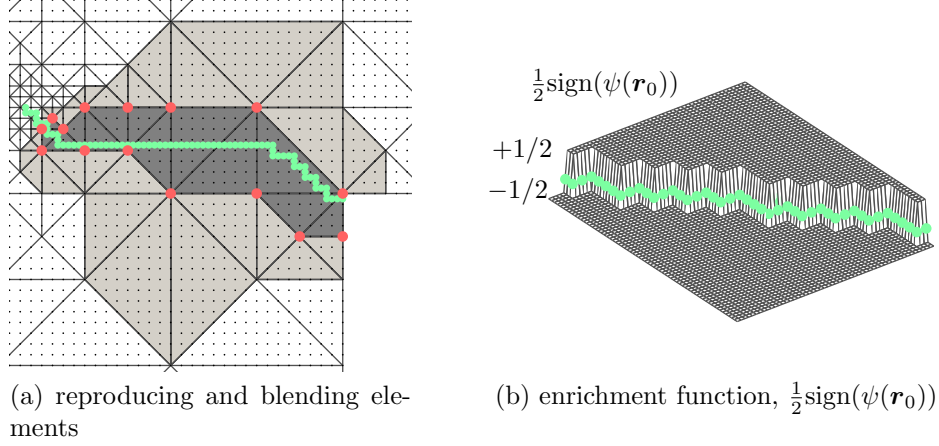


Figure 6: (a) An example of cut or reproducing (dark grey) and blending (light grey) elements. The set of enriched nodes N^* is shown in red dots, and regular atom sites as small black dots. (b) An example of the enrichment function, $\frac{1}{2}\text{sign}(\psi(\mathbf{r}_0^\alpha))$; crack points C are shown as green dots.

In order to incorporate a crack, an enrichment using the local PU concept (standard local XFEM approximation) is introduced. Enrichment terms are included as follows

$$\hat{\mathbf{r}}^\alpha = \hat{\mathbf{r}}_{\text{qc}}^\alpha + \underbrace{\sum_{j=1}^{n^*} \varphi_{\beta_j}(\mathbf{r}_0^\alpha) \frac{1}{2} [\text{sign}(\psi(\mathbf{r}_0^\alpha)) - \text{sign}(\psi(\mathbf{r}_0^{\beta_j}))]}_{\varphi_j^*(\mathbf{r}_0^\alpha)} \hat{\mathbf{g}}_j^*, \quad \alpha \in N_{\text{ato}}, \quad \beta_j \in N^*, \quad (21)$$

where the same P_1 FE shape functions for the extrinsic enrichment terms are used as well.

In Eq. (21), $N^* \subseteq N_{\text{rep}}$ is a set of n^* enriched repatoms associated with the cut elements, φ_j^* denotes the enrichment function of the β_j -th repatom, and $\hat{\mathbf{g}}_j^* \in \mathbb{R}^2$ denotes an admissible vector of generalized DOFs associated with j -th enriched repatom. Let us emphasize that the only enrichment function is $\frac{1}{2}\text{sign}(\psi(\mathbf{r}_0))$, depicted in Fig. 6b, and that the approximation in Eq. (21) yields continuous, piecewise linear interpolation of the displacement jump. Note also that no crack tip enrichments are required, since the crack tip is always located inside the fully resolved region, and that the shifting adopted in Eq. (21) guarantees the Kronecker- δ property of the resulting approximation, cf. Belytschko et al. (2001) or Fries and Belytschko (2010). Furthermore, the shifting implies that there are actually no blending elements, as shifted enrichment functions vanish outside the cut elements. Even when shifting is not adopted, no difficulties with blending elements occur, because the interpolation is based on P_1 FE shape functions and the enrichment function is piecewise constant. For further details see Fries and Belytschko (2010), Sections 4.3 and 5.1.2.

In continuum XFEM, poorly conditioned stiffness matrices occur if the crack path is close to triangle edges and nodes, cf. e.g. Wells and Sluys (2001); Laborde et al. (2005), or Fries and Belytschko (2010). For lattice networks, the measure for closeness is the lattice spacing a . Hence, if a crack path is closer than a to an element edge or node, the resulting system matrix is rendered singular, cf. Fig. 7.

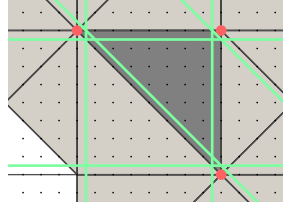


Figure 7: An example of several crack paths (shown as green lines) associated with a cut element (shown in dark grey) that render singular stiffness matrices. Enriched nodes are presented as red dots.

Two approaches are used for continua to remedy this situation. The first approach is the use of clustering (or node gathering) implemented through flat-top functions, cf. e.g. [Fries \(2008\)](#); [Ventura et al. \(2009\)](#); [Babuška and Banerjee \(2012\)](#); [Agathos et al. \(2016b,a\)](#). These techniques usually increase the polynomial order of the resulting approximations if the Kronecker- δ property is required. Hence, this is not desirable within the QC framework, as more extensive changes in the summation rule would be needed.

The second approach is to neglect those φ_j^* that would render the stiffness matrix singular altogether ([Fries and Belytschko, 2010](#), Section 11 and references therein), which is adopted in this contribution. The reason is that such shifted enrichments are identical to zero vector for lattice networks and hence, they provide no additional information to the system.

Finally, upon introducing

$$\Phi_{\text{FE}} = \Phi_{\text{FE},(2\alpha-1)(2j-1)} = \Phi_{\text{FE},(2\alpha)(2j)} = \varphi_{\beta_j}(\mathbf{r}_0^\alpha), \quad \alpha \in N_{\text{ato}}, \quad \beta_j \in N_{\text{rep}}, \quad j = 1, \dots, n_{\text{rep}}, \quad (22)$$

$$\Phi_\star = \Phi_{\star,(2\alpha-1)(2j-1)} = \Phi_{\star,(2\alpha)(2j)} = \varphi_j^\star(\mathbf{r}_0^\alpha), \quad \alpha \in N_{\text{ato}}, \quad j = 1, \dots, n^\star, \quad (23)$$

along with

$$\Phi = [\Phi_{\text{FE}}, \Phi_\star] \quad \text{and} \quad \hat{\mathbf{g}} = [\hat{\mathbf{r}}_{\text{rep}}, \hat{\mathbf{g}}_1^\star, \dots, \hat{\mathbf{g}}_{n^\star}^\star]^\top, \quad (24)$$

the approximation in Eq. (21) takes the form of Eq. (11).

3.3. Summation

The second step of QC frameworks, summation, is the QC counterpart to numerical integration in the finite element method. It serves two purposes. The first one is to estimate the exact system's incremental energy Π^k in an efficient, yet accurate way. This reduces the computational effort related to determining the energies, gradients, and Hessians. The second purpose is to reduce the dimensionality of the internal variable \mathbf{z} , which in combination with the interpolation step realises the reduction of the entire state variable $\mathbf{q}(t_k)$.

3.3.1. General Framework

The exact incremental energy Π^k is approximated using a limited number of site- or interaction-energies and their weight factors. These are typically chosen such that the error of the induced approximation is limited, but a low number of sampling atoms/interactions is required. The interested reader is referred for further details to [Beex et al. \(2011, 2014b\)](#)

for atom-based summation rules, to [Beex et al. \(2015a\)](#) for an interaction-based summation rule, or to [Amelang et al. \(2015\)](#) for an overview of summation rules in atomistic systems.

Here, we employ the central site-energy-based summation rule ([Beex et al., 2014b,c](#)), which considers only the atoms at the element corners plus one near the center. The central one is taken to be representative also of atoms which interact across the element boundaries. If no internal atoms exist, all boundary atoms are considered. The central rule involves a certain degree of approximation, but is significantly more efficient than the exact summation rule not discussed here; for details see ([Beex et al., 2011](#)). The summation rule is implemented by introducing a set of $n_{\text{sam}}^{\text{ato}}$ sampling atoms collected in an index set $S_{\text{ato}} \subseteq N_{\text{ato}}$. The $n_{\text{sam}}^{\text{int}}$ interactions connected to these sampling atoms are stored in an index set S_{int} . Then, the summation step yields the following approximation,

$$\begin{aligned} \Pi^k(\hat{\mathbf{q}}; \mathbf{q}(t_{k-1})) &\approx \hat{\Pi}^k(\hat{\mathbf{q}}; \mathbf{q}(t_{k-1})) = \sum_{\alpha \in S_{\text{ato}}} w_{\alpha} \pi_{\alpha}^k(\hat{\mathbf{q}}; \mathbf{q}(t_{k-1})) - \mathbf{f}_{\text{ext}}^{\top} \hat{\mathbf{r}} \\ &= \sum_{\alpha \beta \in S_{\text{int}}} \tilde{w}_{\alpha \beta} \tilde{\pi}_{\alpha \beta}^k(\hat{\mathbf{q}}; \mathbf{q}(t_{k-1})) - \mathbf{f}_{\text{ext}}^{\top} \hat{\mathbf{r}}, \end{aligned} \quad (25)$$

where w_{α} are the weight factors associated with atom sites, and $\tilde{w}_{\alpha \beta}$ are corresponding weight factors associated with interactions.

Because the approximate incremental energy in Eq. (25) only depends on the internal variables associated with $n_{\text{sam}}^{\text{int}}$ interactions, one can introduce a reduced state variable of the QC system in the form $\mathbf{q}_{\text{red}}(t_k) = (\mathbf{g}(t_k), \mathbf{z}_{\text{sam}}(t_k)) \in \mathcal{Q}_{\text{red}}(t_k)$, where $\mathbf{z}_{\text{sam}} \in \mathbb{R}^{n_{\text{sam}}^{\text{int}}} = \mathcal{Z}_{\text{sam}}$ is a column that stores the internal variables of all sampling interactions. The reduced state space then reads $\mathcal{Q}_{\text{red}}(t_k) = \mathcal{G}(t_k) \times \mathcal{Z}_{\text{sam}}$.

3.3.2. Summation Rule for Enrichment Functions

If the enrichment of Section 3.2.4 is adopted and a coarse triangle is cut by a crack, Eq. (25) still holds, but the selection of the individual sampling atoms S_{ato} and their weights w_{α} changes.

In the central summation rule, all crack wake atoms are treated as additional triangle edges. Therefore, a cut triangle is split into two regions, bounded by triangle edges and one crack face. For each of the two subregions, the standard central summation rule is used. Hence, if no internal atoms exist, all edge atoms are added as discrete sampling atoms. Otherwise, a central sampling atom is selected with the weight corresponding to the sum of the number of internal atoms plus one half of the number of edge atoms. Atoms at edge intersections are added as discrete sampling atoms. For the detailed algorithmic description and pictorial representation see Alg. 1 and Fig. 8.

Note that the above-described summation rule, which in its current form does not take into account crack closure (recall Eq. (5) and the discussion therein), can be easily generalized to deal also with non-monotonous loading and crack closure merely by adding all crack wake atoms N_{cw} as discrete sampling atoms. Special summation rule that samples crack faces can also be devised, but this is omitted from our further considerations for the sake of simplicity. Because only monotonous loading and crack opening are observed in examples Section 5, the summation rule presented in Alg. 1 is adequate yet efficient.

Algorithm 1: Central summation rule for cut elements.

- 1: Identify crack wake atoms $N_{\text{cw}} = \{\alpha, \beta \mid \omega^{\alpha\beta} \geq \eta\}$.
- 2: **for each triangle** $K \in \mathcal{T}_k$
 - (I): **If** triangle is not cut by a crack, use standard central summation rule (Beex et al., 2014b).
 - (II): **Else**
 - (i): Identify triangle's internal N_i^K , edge N_e^K , vertex N_v^K , and all N^K , atoms.
 - (ii): Select vertex atoms N_v^K as discrete sampling atoms ($w_\alpha = 1$).
 - (iii): **If** no internal atoms exist, select all atoms N^K as discrete sampling atoms ($w_\alpha = 1$).
 - (iv): **Else**
 - (a): Split N^K in sets N_+^K and N_-^K according to the sign of ψ .
 - (b): Define $\tilde{N}_i^K = N_i^K \setminus N_{\text{cw}}^K$. Split \tilde{N}_i^K into two disjoint sets $\tilde{N}_{i,+}^K$ and $\tilde{N}_{i,-}^K$ according to the sign of ψ and sort both with respect to the number of neighbours inside triangle (in decreasing order).
 - (c): **If** $\tilde{N}_{i,\pm}^K$ is empty, all atoms in $N_\pm^K \setminus N_v^K$ are discrete sampling atoms.
 - (d): **Else**
 - Choose $\beta = \tilde{N}_{i,\pm}^K(1)$ as central sampling atom.
 - For each $\alpha \in \tilde{N}_{i,\pm}^K$, $w_\beta = w_\beta + 1$.
 - Add all $\alpha \in (N_{\text{cw}} \cap N_e^K)$ as discrete sampling atoms ($w_\alpha = 1$).
 - Identify discrete sampling atoms on edges resulting from neighbouring triangles \tilde{N}_e^K .
 - For each $\alpha \in (N_\pm^K \setminus (N_v^K \cup \tilde{N}_{i,\pm}^K \cup \tilde{N}_e^K \cup (N_{\text{cw}} \cap N_e^K)))$, $w_\beta = w_\beta + 0.5$.
- 3: **end**

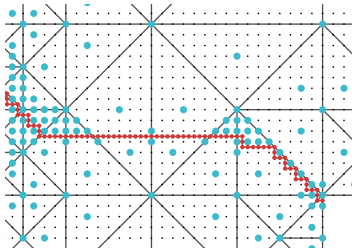


Figure 8: Schematic representation of the set of sampling atoms contained in S_{ato} for the central summation rule. Large blue dots represent the sampling atoms, and the crack points C from (9) are shown as red dots.

Algorithm 2: X-QC algorithm.

- 1: Initialize the system: apply initial condition \mathbf{q}_0 and construct initial (coarse) mesh \mathcal{T}_0 with required information, e.g. $N_{\text{rep}}(t_0)$, $\Phi(t_0)$, $S_{\text{ato}}(t_0)$, $S_{\text{int}}(t_0)$.
- 2: **for** $k = 1, \dots, n_T$
 - (i): Apply the boundary conditions at time t_k , $\mathcal{T}_k = \mathcal{T}_{k-1}$, $N_{\text{rep}}(t_k) = N_{\text{rep}}(t_{k-1})$, $\Phi(t_k) = \Phi(t_{k-1})$, $S_{\text{ato}}(t_k) = S_{\text{ato}}(t_{k-1})$, $S_{\text{int}}(t_k) = S_{\text{int}}(t_{k-1})$, etc.
 - (ii): Equilibrate the unbalanced system, i.e. solve for $\mathbf{q}_{\text{red}}(t_k) \in \mathcal{Q}_{\text{red}}(t_k)$ using $\hat{\Pi}^k(\hat{\mathbf{q}}_{\text{red}}; \mathbf{q}_{\text{red}}(t_{k-1}))$ of Eq. (25). Update crack description ψ , C , etc.
 - (iii): For each element $K \in \mathcal{T}_k$ evaluate its refinement indicator in (15) and construct $\mathcal{I}_r \subseteq \mathcal{T}_k$. If $\mathcal{I}_r \neq \emptyset$ refine and update \mathcal{T}_k .
 - (iv): Protect newly added repatoms from all previous refinements during the current time step t_k ; if necessary, protect also other repatoms, e.g. those near the crack tip. Use (17) to identify $\mathcal{I}_c \subseteq \mathcal{T}_k$. If possible, coarsen and update \mathcal{T}_k .
 - (v): **If** \mathcal{T}_k changed in (iii) – (iv), update the system information $N_{\text{rep}}(t_k)$, $\Phi(t_k)$, $S_{\text{ato}}(t_k)$, $S_{\text{int}}(t_k)$, etc., and return to (ii) since the system is unbalanced.
Else if the mesh has converged; proceed to (vi).
 - (vi): Store relevant outputs: $\mathbf{q}_{\text{red}}(t_k)$, \mathcal{T}_k , $N_{\text{rep}}(t_k)$, $\Phi(t_k)$, $S_{\text{ato}}(t_k)$, $S_{\text{int}}(t_k)$, C , etc.
- 3: **end**

3.4. X-QC

In all previous Sections 3.1 – 3.3, we have assumed an existing crack and triangulation \mathcal{T}_k . We are, however, interested in evolving crack tips and fully resolved regions. Therefore, we summarize the mesh refinement, coarsening, and additions of enrichments of the total X-QC framework in Alg. 2.

3.5. Energy Implications

This section discusses the implications of the adaptive scheme summarized in Alg. 2 from an energetic point of view, and extends the discussion presented in Rokoš et al. (2016b), Section 3.5. Recall that the motivations for energy considerations are threefold. First, the entire theory presented so far is based on energy minimization and the adaptive procedure should be consistent with these principles. Second, validity of the solution $\mathbf{q}(t_k)$, as well as of $\mathbf{q}_{\text{red}}(t_k)$, is decided based on the energy balance (E), which must hold during the entire evolution of the system. Finally, upon taking into account energy implications, the accuracy of the X-QC framework can be assessed from the energetic point of view.

The issue focused on here is illustrated in Fig. 9. At the end of the previous time step t_{k-1}^+ , the system is relaxed for some mesh \mathcal{T}_{k-1}^+ . After the next increment is applied for mesh $\mathcal{T}_k^- = \mathcal{T}_{k-1}^+$ and the system is equilibrated (stage (ii) of Alg. 2), refinement and coarsening may be required ((ii) – (iv)). Upon convergence, this yields a triangulation \mathcal{T}_k^+ . In order to accurately construct the energy increments, one should distinguish physical increments, computed on mesh \mathcal{T}_{k-1}^+ and denoted with subscripts "P", and changes in energy which are due to the mesh adaptation from \mathcal{T}_k^- to \mathcal{T}_k^+ , denoted with subscripts "A". The artificial

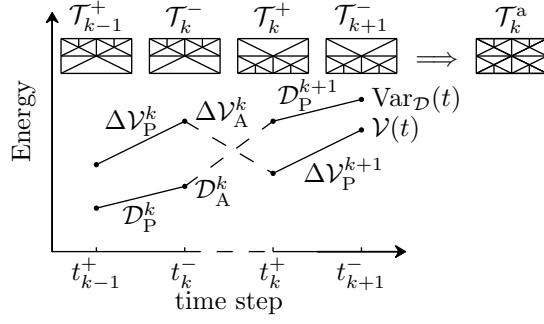


Figure 9: Sketch of possible energy evolutions during time step t_k when refinement and coarsening occur. Only the $\mathcal{V}(t)$ and $\text{Var}_{\mathcal{D}}(t)$ components are shown for clarity.

energy increments due to mesh adaptation are computed by projecting converged solutions onto an artificial mesh \mathcal{T}_k^a , which establishes communication between the two systems (note that these two systems have different numbers of DOFs and internal variables). The artificial mesh therefore contains the union of repatoms and sampling interactions present in both systems and hence, it is locally the finest triangulation of the two, cf. Fig. 9. Using the above-described procedure and evaluating energies at time instants t_k^+ provides energy profiles that we will call *reconstructed*. For further details see [Rokoš et al. \(2016b\)](#), Section 3.5.

Let us note that we omit dissipative coarsening (i.e. the interpolation of the internal variables when the mesh is coarsened), and assume that the coarsening occurs only in elastic regions. This assumption is reasonable because damage is localized. Consequently, all damaged bonds are captured accurately by the special function enrichments and associated summation rule.

4. Solution Strategy

In this section, we discuss the minimization of the reduced incremental energy $\hat{\Pi}^k$ in (IP), considered in step (ii) of Alg. 2. A fixed triangulation \mathcal{T}_k is again assumed. For the solution of the DNS, the interested reader is referred to [Rokoš et al. \(2016b\)](#), Section 4.1.

We first reduce the incremental energy

$$\hat{\Pi}_{\text{red}}^k(\hat{\mathbf{g}}; \mathbf{q}_{\text{red}}(t_{k-1})) = \min_{\hat{\mathbf{z}}_{\text{sam}} \in \mathcal{Z}_{\text{sam}}} \hat{\Pi}^k(\hat{\mathbf{g}}, \hat{\mathbf{z}}_{\text{sam}}; \mathbf{q}_{\text{red}}(t_{k-1})), \quad (26)$$

see e.g. [Mielke and Roubíček \(2015\)](#), Section 3.1.2, or [Carstensen et al. \(2002\)](#), and rewrite (IP) as

$$\mathbf{g}(t_k) = \arg \min_{\hat{\mathbf{g}} \in \mathcal{G}(t_k)} \hat{\Pi}_{\text{red}}^k(\hat{\mathbf{g}}; \mathbf{q}_{\text{red}}(t_{k-1})). \quad (\text{IP}_{\text{red}})$$

Second, (IP_{red}) is solved by a standard Newton algorithm because $\hat{\Pi}_{\text{red}}^k$ is assumed to be smooth enough in $\hat{\mathbf{g}}$. Using the chain rule in the Taylor expansion of $\hat{\Pi}_{\text{red}}^k$, the following stationarity condition is obtained:

$$\mathbf{H}^i(\hat{\mathbf{g}}^{i+1} - \hat{\mathbf{g}}^i) + \mathbf{G}^i = \mathbf{0}, \quad (27)$$

where

$$\mathbf{G}^i = \mathbf{G}(\hat{\mathbf{g}}^i) = \mathbf{\Phi}^\top(t_k) \frac{\partial \hat{\Pi}_{\text{red}}^k(\hat{\mathbf{r}}; \mathbf{q}_{\text{red}}(t_{k-1}))}{\partial \hat{\mathbf{r}}} \bigg|_{\hat{\mathbf{r}} = \mathbf{\Phi}(t_k) \hat{\mathbf{g}}^i}, \quad (28a)$$

$$\mathbf{H}^i = \mathbf{H}(\hat{\mathbf{g}}^i) = \mathbf{\Phi}^\top(t_k) \frac{\partial^2 \hat{\Pi}_{\text{red}}^k(\hat{\mathbf{r}}; \mathbf{q}_{\text{red}}(t_{k-1}))}{\partial \hat{\mathbf{r}} \partial \hat{\mathbf{r}}} \mathbf{\Phi}(t_k) \bigg|_{\hat{\mathbf{r}} = \mathbf{\Phi}(t_k) \hat{\mathbf{g}}^i}. \quad (28b)$$

The partial derivatives in Eqs. (28) read

$$\frac{\partial \hat{\Pi}_{\text{red}}^k(\hat{\mathbf{r}}; \mathbf{q}_{\text{red}}(t_{k-1}))}{\partial \hat{\mathbf{r}}} = -\mathbf{f}_{\text{ext}}(t_k) + \sum_{\alpha \in S_{\text{ato}}(t_k)} w_\alpha \frac{\partial \pi_{\text{red},\alpha}^k(\hat{\mathbf{r}}; \mathbf{q}_{\text{red}}(t_{k-1}))}{\partial \hat{\mathbf{r}}} \quad (29a)$$

$$= -\mathbf{f}_{\text{ext}}(t_k) + \sum_{\alpha \in S_{\text{ato}}(t_k)} w_\alpha \mathbf{f}_{\text{int}}^\alpha(\hat{\mathbf{r}}),$$

$$\frac{\partial^2 \hat{\Pi}_{\text{red}}^k(\hat{\mathbf{r}}; \mathbf{q}_{\text{red}}(t_{k-1}))}{\partial \hat{\mathbf{r}} \partial \hat{\mathbf{r}}} = \sum_{\alpha \in S_{\text{ato}}(t_k)} w_\alpha \frac{\partial^2 \pi_{\text{red},\alpha}^k(\hat{\mathbf{r}}; \mathbf{q}_{\text{red}}(t_{k-1}))}{\partial \hat{\mathbf{r}} \partial \hat{\mathbf{r}}} = \sum_{\alpha \in S_{\text{ato}}(t_k)} w_\alpha \mathbf{K}^\alpha(\hat{\mathbf{r}}), \quad (29b)$$

where the reduced site energies, $\pi_{\text{red},\alpha}^k$, are introduced in analogy to (26) by condensing out the internal variables. Eq. (27) presents a system of linear equations for increments $\hat{\mathbf{g}}^{i+1} - \hat{\mathbf{g}}^i$, and iterating Eqs. (27) and (28) until convergence of $\|\mathbf{G}^i\|_2$ yields $\mathbf{g}(t_k)$.

Note that explicit expressions for the gradients and Hessians can be found in Rokoš et al. (2016a), Appendix A. Here, the quantities are derived for lattice structures with isotropic hardening plasticity and hence they have to be multiplied by $(1 - \omega^{\alpha\beta})$ if a bond is loaded in tension. Moreover, the dependencies on all plastic internal variables have to be dropped.

Before the gradient and Hessian in Eqs. (28) are computed, the approximate incremental energy must be minimized with respect to $\hat{\mathbf{z}}_{\text{sam}}$ according to Eq. (26). To this end, the interaction-based formulation of the incremental energy specified in Eq. (25) is used. The minimization then results in $n_{\text{sam}}^{\text{int}}$ independent one-dimensional box-constrained minimization problems

$$\hat{\omega}^{\alpha\beta,i} = \arg \min_{\omega^{\alpha\beta}(t_{k-1}) \leq \hat{\omega}^{\alpha\beta} \leq 1} \tilde{w}_{\alpha\beta} \tilde{\pi}_{\alpha\beta}^k(\hat{\mathbf{r}}^{\alpha\beta,i}, \hat{\omega}^{\alpha\beta}; \mathbf{q}(t_{k-1})), \quad \alpha\beta \in S_{\text{int}}(t_k). \quad (30)$$

For further details see Rokoš et al. (2016b), Section 4.1 and Appendix A.

5. Numerical Examples

In this section the framework is applied to two examples discussed already in Rokoš et al. (2016b), where coarsening was not considered. Consequently, we can make a direct comparison in terms of accuracy and efficiency between the adaptive QC frameworks with and without coarsening.

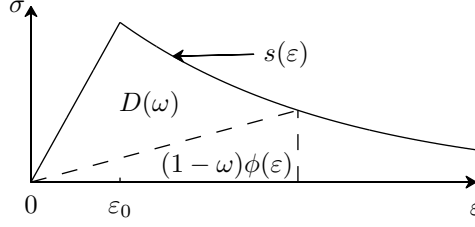


Figure 10: Exponential softening under tension: a sketch of the stress–strain diagram with corresponding quantities ε_0 and $s(\varepsilon)$, cf. Eq. (32). The elastically stored energy, $(1 - \omega)\phi(\varepsilon)$, corresponds to the area of the dashed triangle, and the dissipated energy, $D(\omega)$, to the area of the upper triangle with the curved edge.

Table 1: Dimensionless material and geometric parameters for both examples.

Physical parameters		Example 1	Example 2
Young’s modulus,	E	1	1
Cross-sectional area,	A	1	1
Lattice spacing,	a_x, a_y	1	1
Limit elastic strain,	ε_0	0.1	0.01
Initial slope,	ε_f	0.25	0.025
Indirect displacement increment, $\overline{\Delta\ell}$		0.025	see Fig. 18a

The same material model is used for each lattice spring (the superscripts $\alpha\beta$ are dropped for brevity):

$$\phi(\hat{r}) = \frac{1}{2}EA r_0 (\hat{\varepsilon}(\hat{r}))^2, \quad (31)$$

where E is the Young’s modulus, A the cross-sectional area, and $\hat{\varepsilon} = (\hat{r} - r_0)/r_0$ the bond strain. The dissipation function D in Eq. (6) is adopted from Rokoš et al. (2016b), Appendix A, providing an exponential softening rule

$$\hat{\sigma} = s(\hat{\varepsilon}) = E\varepsilon_0 \exp\left(-\frac{\hat{\varepsilon} - \varepsilon_0}{\varepsilon_f}\right), \quad \varepsilon_0 \leq \hat{\varepsilon}. \quad (32)$$

In Eq. (32), $s(\hat{\varepsilon})$ describes the softening branch of the associated stress-strain diagram, $\hat{\sigma}$ is the bond stress, ε_f measures the initial slope of the softening branch, and ε_0 is the limit elastic strain, cf. Fig. 10. The employed parameters are specified in Tab. 1.

5.1. L-Shaped Plate Example

The first example focuses on an L-shaped plate test, see Fig. 11. The lattice properties are homogeneous except for the vicinity of $\Gamma_3/2$, where a vertical displacement is applied. Here,

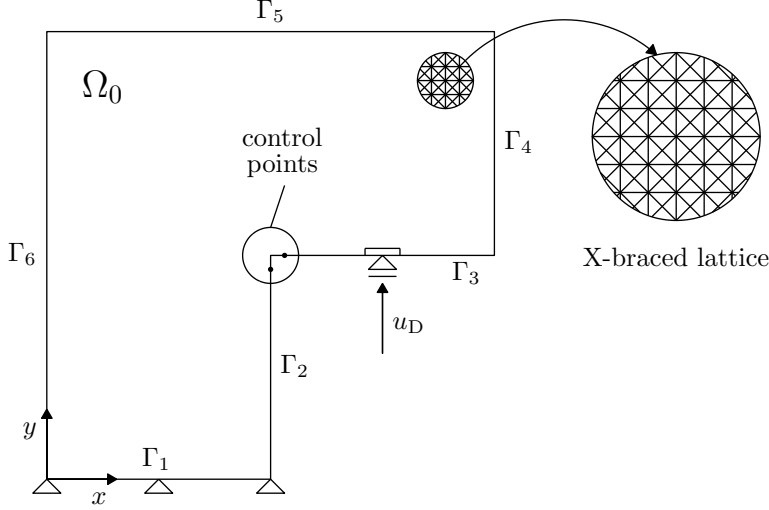


Figure 11: Sketch of the L-shaped plate example: geometry and boundary conditions. Variable u_D denotes the applied vertical displacement.

in order to prevent any damage, the Young's modulus is 1,000 times larger than elsewhere and the limit elastic strain ε_0 is infinite. The reference domain comprises 3,201 atoms, 12,416 interactions, and is fixed at the bottom part of the boundary, Γ_1 . The evolution of the system is controlled by the Crack Mouth Opening Displacement (CMOD) through a pair of crack tip atoms highlighted in Fig. 11.

The numerical simulation is performed for two X-QC systems, each with a different safety margin θ_r , cf. Eqn. (14). The first system is referred to as the *moderate X-QC* ($\theta_r = 0.5$) and the second one to as the *progressive X-QC* ($\theta_r = 0.25$); in both cases, $\theta_c = 0.05$, recall Eq. (16). Relatively low safety margins are necessary due to the highly fluctuating interaction energies near the crack tip (recall Fig. 4 and the discussion therein). The results are compared to those of the adaptive version of the variational QC, reported in Rokoš et al. (2016b), for the same choices of the refinement safety margins, i.e. $\theta_r = 0.5$ and $\theta_r = 0.25$, and for the central summation rule. These systems are referred to as the *moderate adaptive QC* and the *progressive adaptive QC*. For completeness, results of the DNS are also shown.

The deformed configuration computed by the DNS at $u_D = 14$ is depicted in Fig. 12a. The crack path initiates at the inner corner ($\Gamma_2 \cap \Gamma_3$) and propagates to the left. This is also predicted by the QC frameworks. In Fig. 12b, the reaction force F is presented as a function of u_D . The responses predicted by the X-QC are practically identical to those of the adaptive QC without coarsening.

The energy profiles appear in Fig. 13a as functions of u_D . The energy balance (E) is clearly satisfied along the entire loading path, i.e. the thin dotted lines presenting the work performed by external forces \mathcal{W}_{ext} lie on top of the thick dashed lines representing $\mathcal{V} + \text{Var}_{\mathcal{D}}$. Second, similarly to the reaction force profiles, we notice that the energy paths are almost indistinguishable from those of adaptive QC, demonstrating good accuracy of the X-QC approach. In Fig. 13b, we present the energy components that are exchanged (the artificial

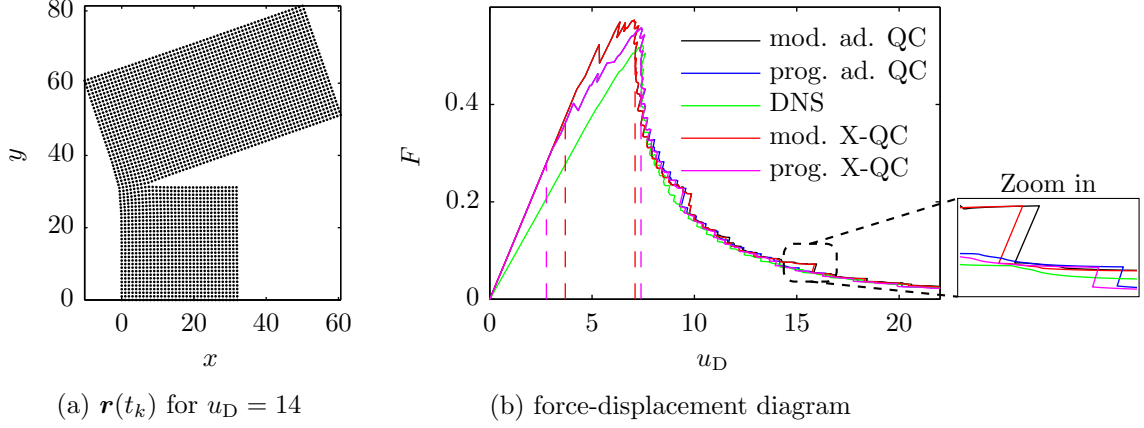


Figure 12: L-shaped plate test: (a) the deformed (unscaled) configuration at $u_D = 14$ predicted by the DNS, (b) the force-displacement diagram for the reaction force F as a function of u_D . The instants at which mesh refinement and coarsening occur for the first time are indicated by dashed vertical lines of the respective colours.

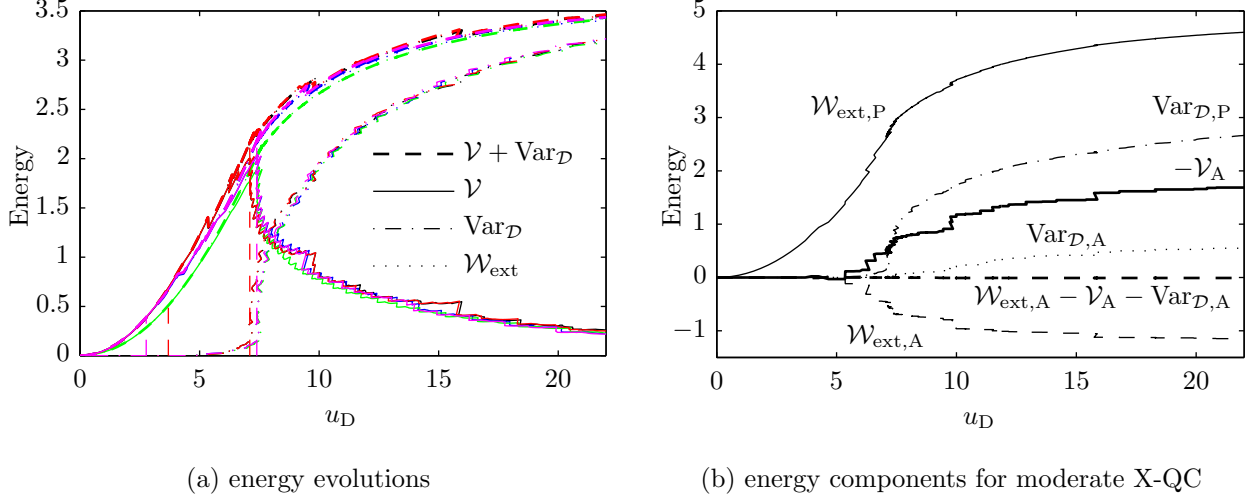


Figure 13: Energy profiles for the L-shaped plate test. (a) The energy evolutions (black – the moderate adaptive QC, blue – the progressive adaptive QC, green – DNS, red – moderate X-QC, magenta – progressive X-QC). (b) Energy exchanges due to mesh refinement and coarsening for the moderate X-QC approach, cf. Section 3.5.

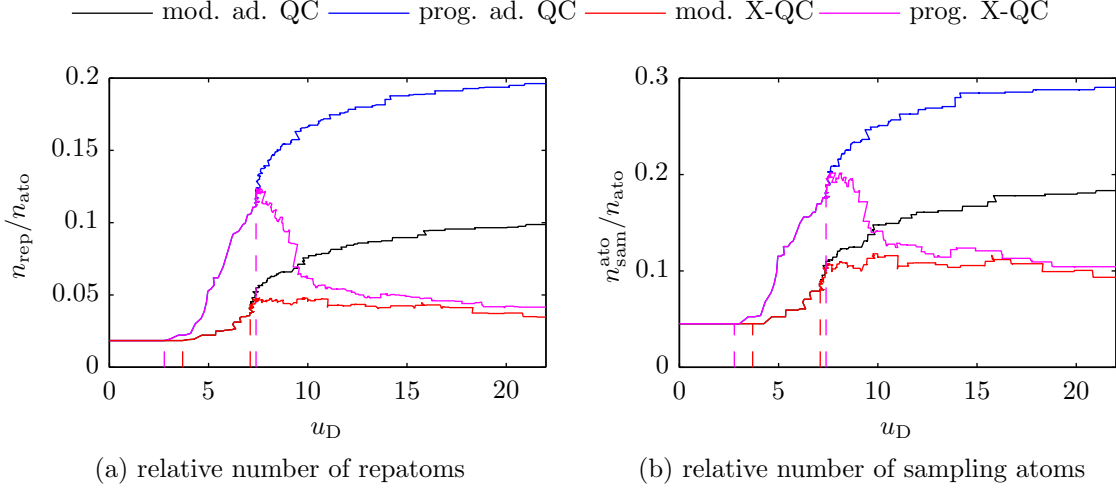


Figure 14: (a) Relative number of repatoms $n_{\text{rep}}/n_{\text{ato}}$ as a function of u_D , and (b) relative number of sampling atoms.

energies) in the moderate X-QC simulation. Their high magnitudes compared to the curves of Fig. 13a indicate the importance of the energy reconstruction procedure, discussed in Section 3.5.

Fig. 14a presents the relative number of repatoms as a function of u_D . Note that the number of enriched repatoms n^* , defined in Eq. (21), is negligible (in particular, $n^*/n_{\text{rep}} < 0.06$). Both X-QC systems initially follow the trends of the corresponding adaptive QC systems (the refinement stage and crack localization). After the crack localizes and starts to propagate however, the crack wake unloads and the mesh coarsens, resulting in a substantial drop in the number of repatoms of the progressive X-QC. At the end of the simulation, the specimen is almost stress-free, allowing for a very coarse representation. Note that the number of DOFs associated with the X-QC approach is less than one half compared to the adaptive QC in the case of the moderate approach, and approximately a quarter in the case of the progressive approach. In both cases, the final relative number of DOFs as well as repatoms remain below 5%, whereas they never exceed 15% during the simulation. A similar behaviour can be observed also for the relative number of sampling atoms, presented in Fig. 14b.

Finally, Figs. 15 and 16 present some of the meshes of the X-QC and the adaptive QC frameworks associated with Fig. 14. Although at the initial stages the progressive and moderate X-QC meshes differ substantially, they are almost identical when the crack localizes. The effect of coarsening in both cases is evident. Note that in the progressive case coarsening occurs not only along the crack path, but also along the right edge of the lower part of the plate. This explains the particularly large gain in number of repatoms in this case, i.e. the factor of four visible in Fig. 14a.

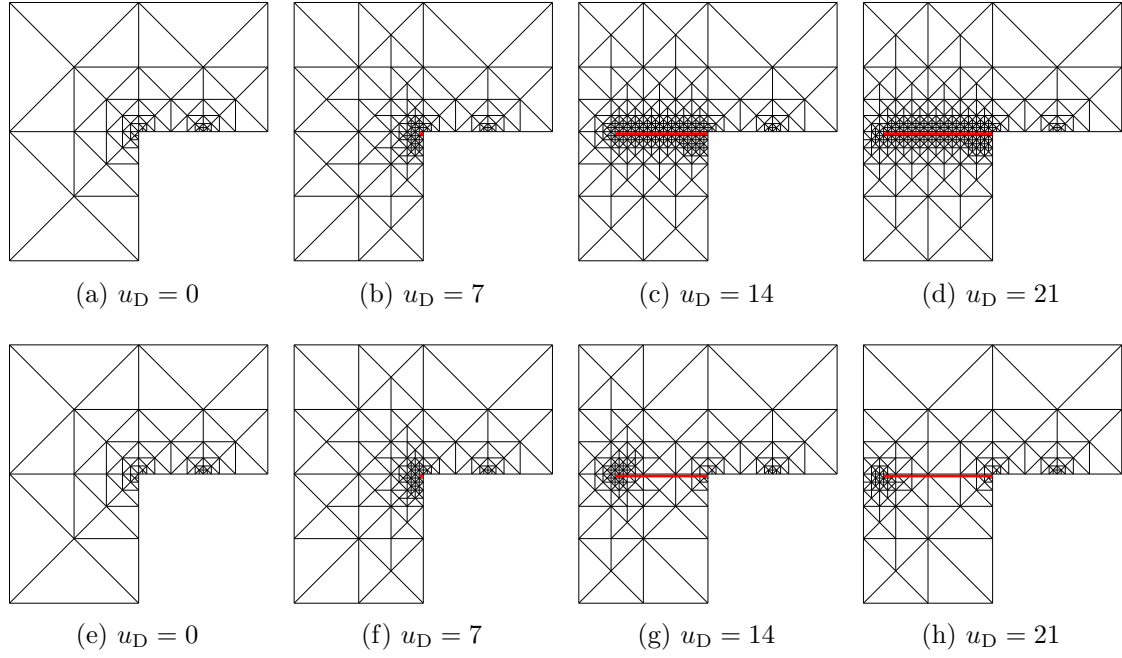


Figure 15: Eight triangulations for the L-shaped plate test: (a) – (d) the moderate adaptive QC approach, (e) – (h) the moderate X-QC approach. The red line indicates the crack. The relative numbers of repatoms and sampling atoms corresponding to these meshes are shown in Fig. 14.

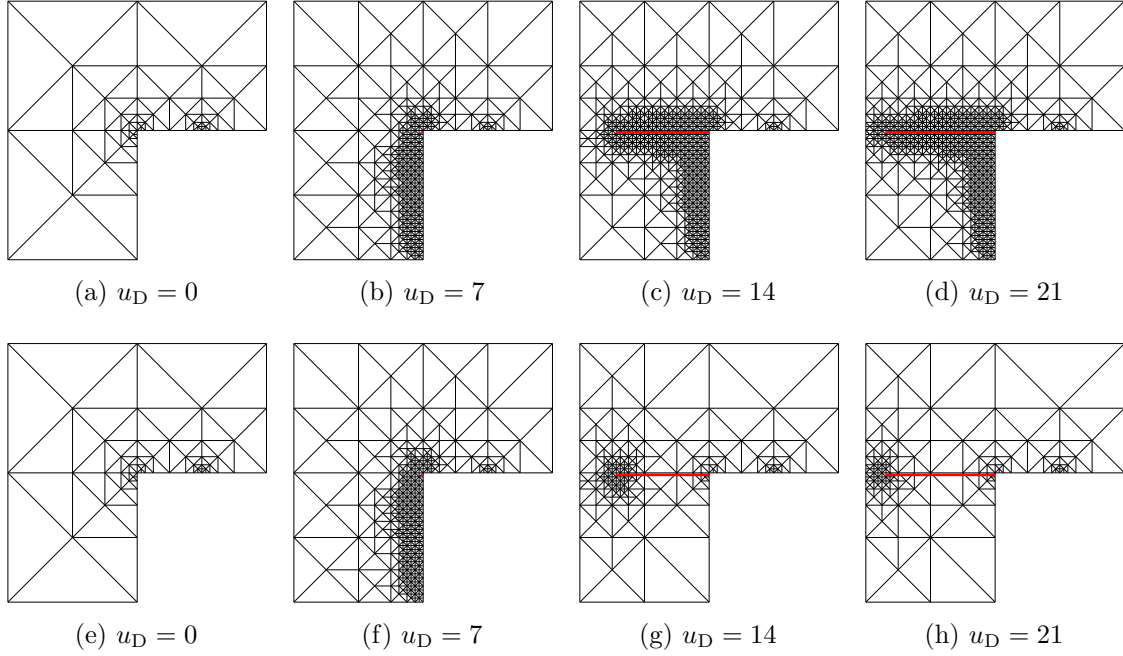


Figure 16: Eight triangulations for the L-shaped plate test: (a) – (d) the progressive adaptive QC approach, (e) – (h) the progressive X-QC approach. The red line indicates the crack. The relative numbers of repatoms and sampling atoms corresponding to these meshes are shown in Fig. 14.

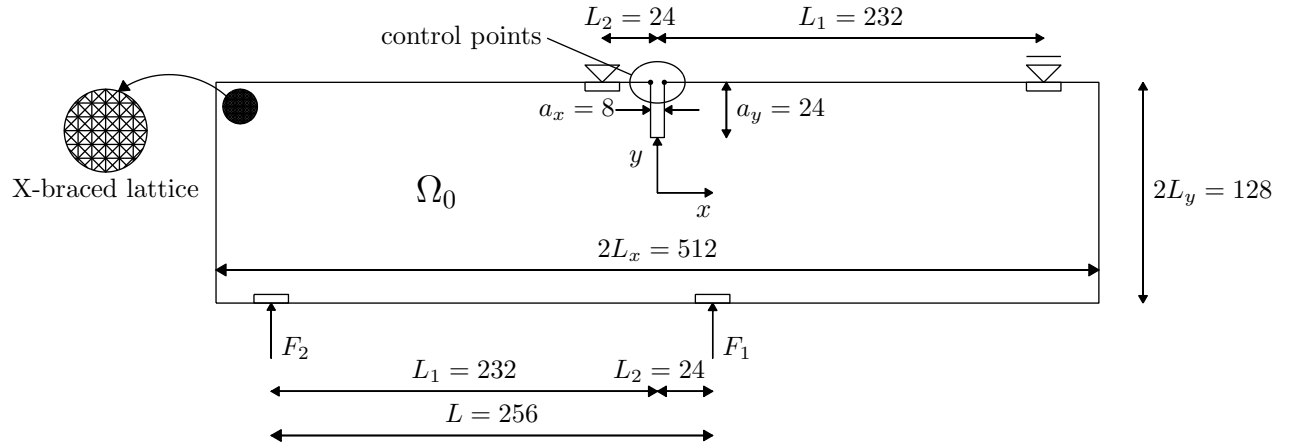


Figure 17: Sketch of the four-point bending test: geometry and boundary conditions.

5.2. Antisymmetric Four-Point Bending Test

The second example is a four-point bending test, presented e.g. in [Schlangen \(1993\)](#), cf. also Fig. 17. The rectangular reference domain Ω_0 is pre-notched at the top to initiate a crack. The otherwise homogeneous X-braced lattice is again locally stiffened where the Dirichlet and Neumann boundary conditions are applied (the Young's modulus is 1,000 times larger than elsewhere and the limit elastic strain ε_0 is infinite to prevent damage). The domain comprises 66,009 atoms connected by 262,040 interactions and is loaded by a pair of vertical forces F_1 and F_2 , given by

$$F_1 = \frac{L_1}{L}\lambda, \quad F_2 = \frac{L_2}{L}\lambda, \quad (33)$$

where λ represents the indirect displacement control parameter, see e.g. [Jirásek and Bažant 2002](#), Section 22.2.3. Unlike the L-shaped plate example, the sum of CMOD and CMSD (Crack Mouth Sliding Displacement) is now used to control the simulation. In Fig. 18a the loading program is specified.

Again two X-QC systems are studied: the moderate X-QC with $\theta_r = 0.5$, and the progressive X-QC with $\theta_r = 0.25$. The results are again compared to those of the adaptive QC (with the same values of θ_r) and to those of the DNS.

The deformed configuration predicted by the DNS at $\text{CMOD} + \text{CMSD} = 5.5$ is depicted in Fig. 18b. The X-QC crack paths, shown in Fig. 19a, are practically identical to those of the adaptive QC (the maximum distance amounts to one lattice spacing). They also match the crack path predicted by the DNS, where the distance does not exceed four lattice spacings in all cases. The same quality of approximation is achieved also for the total applied force, $F_1 + F_2$, plotted in Fig. 19b against $\text{CMOD} + \text{CMSD}$. Some minor differences can be observed between the responses of the X-QC and the adaptive QC around the peak load (when the crack localizes). At this stage, the X-QC meshes start to coarsen. At later stages, all curves become practically indistinguishable as the specimen becomes stress-free.

The energy profiles for all employed approaches are presented in Fig. 20a. The energy balance (E) clearly holds. One can also notice that the X-QC energies match the adaptive QC and DNS energies well. In Fig. 20b the energy exchanges of the moderate X-QC approach are shown. Again, like in the previous example, their contributions are substantial.

In Fig. 21a, the relative number of repatoms of the QC schemes are shown as a function of $\text{CMOD} + \text{CMSD}$. The number of enriched repatoms is again negligible compared to the number of repatoms ($n^*/n_{\text{rep}} < 0.03$). Before the crack localizes, the number of repatoms rapidly increases. But it drops significantly after crack localization, and converges to approximately 1 % for both X-QC approaches. Similar behaviour can be observed for the relative number of sampling atoms shown in Fig. 21b. This result, in combination with the accuracy captured by Figs. 19 and 20a, clearly demonstrates the strength of the X-QC framework. Finally, in Figs. 22 and 23 several snapshots capturing the evolution of the triangulations \mathcal{T}_k are presented.

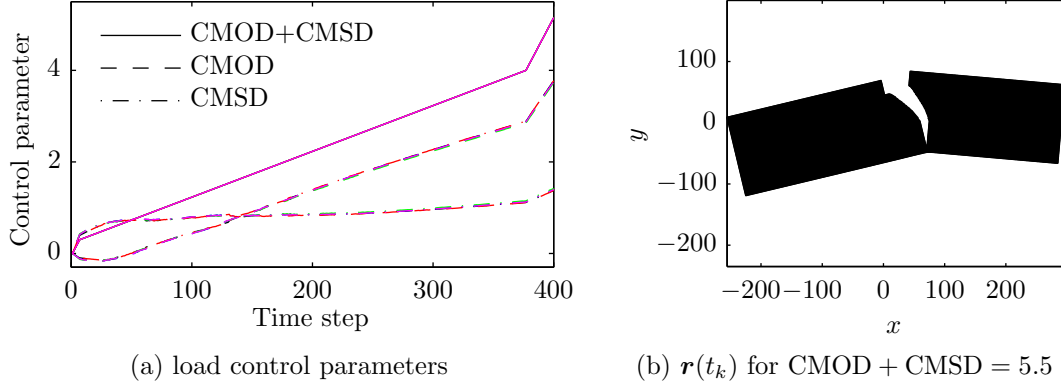


Figure 18: Four-point bending test: (a) evolution of CMOD, CMSD, and their sum (the applied loading program); black – the moderate adaptive QC, blue – the progressive adaptive QC, green – DNS, red – moderate X-QC, magenta – progressive X-QC (note that they are almost indistinguishable). (b) The deformed configuration for the DNS; displacements are magnified by a factor of 10.

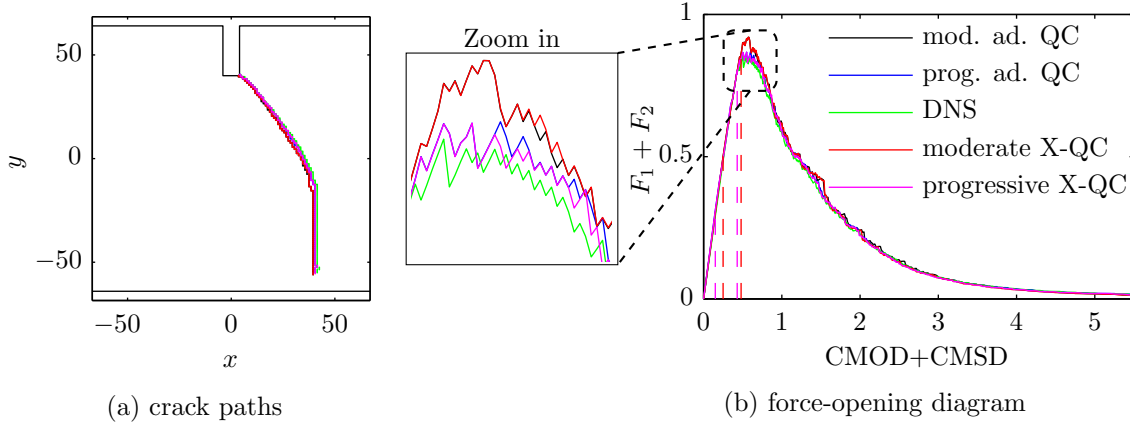


Figure 19: Four-point bending test: (a) crack paths, and (b) force-opening diagram, i.e. $\lambda = F_1 + F_2$ versus CMOD+CMSD. Note that the colour scheme applies to both diagrams. The instants at which mesh refinement and coarsening occur for the first time are indicated by vertical dashed lines of the respective colours.

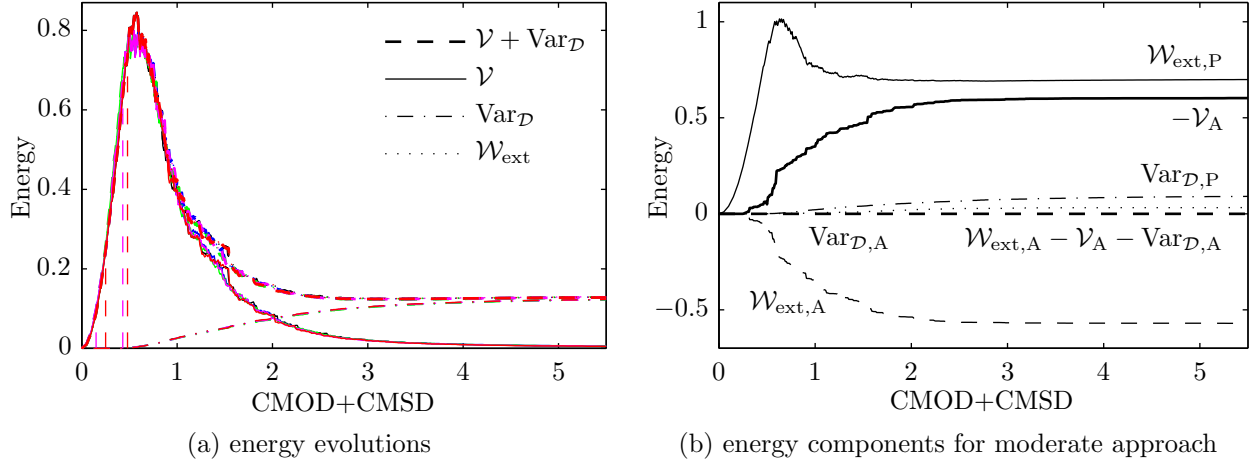


Figure 20: Four-point bending test. (a) Energy evolutions (black – the moderate adaptive QC, blue – the progressive adaptive QC, green – DNS, red – moderate X-QC, magenta – progressive X-QC). (b) Energies exchanged during mesh refinement and coarsening for the moderate QC approach, cf. Section 3.5.

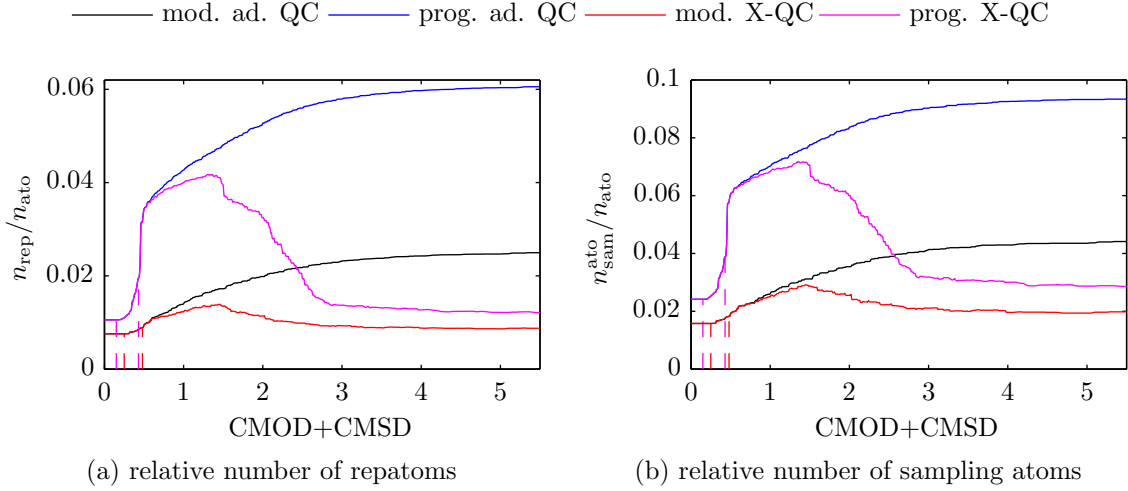


Figure 21: (a) Relative number of repatoms $n_{\text{rep}}/n_{\text{ato}}$ as a function of CMOD + CMSD, and (b) relative number of sampling atoms.

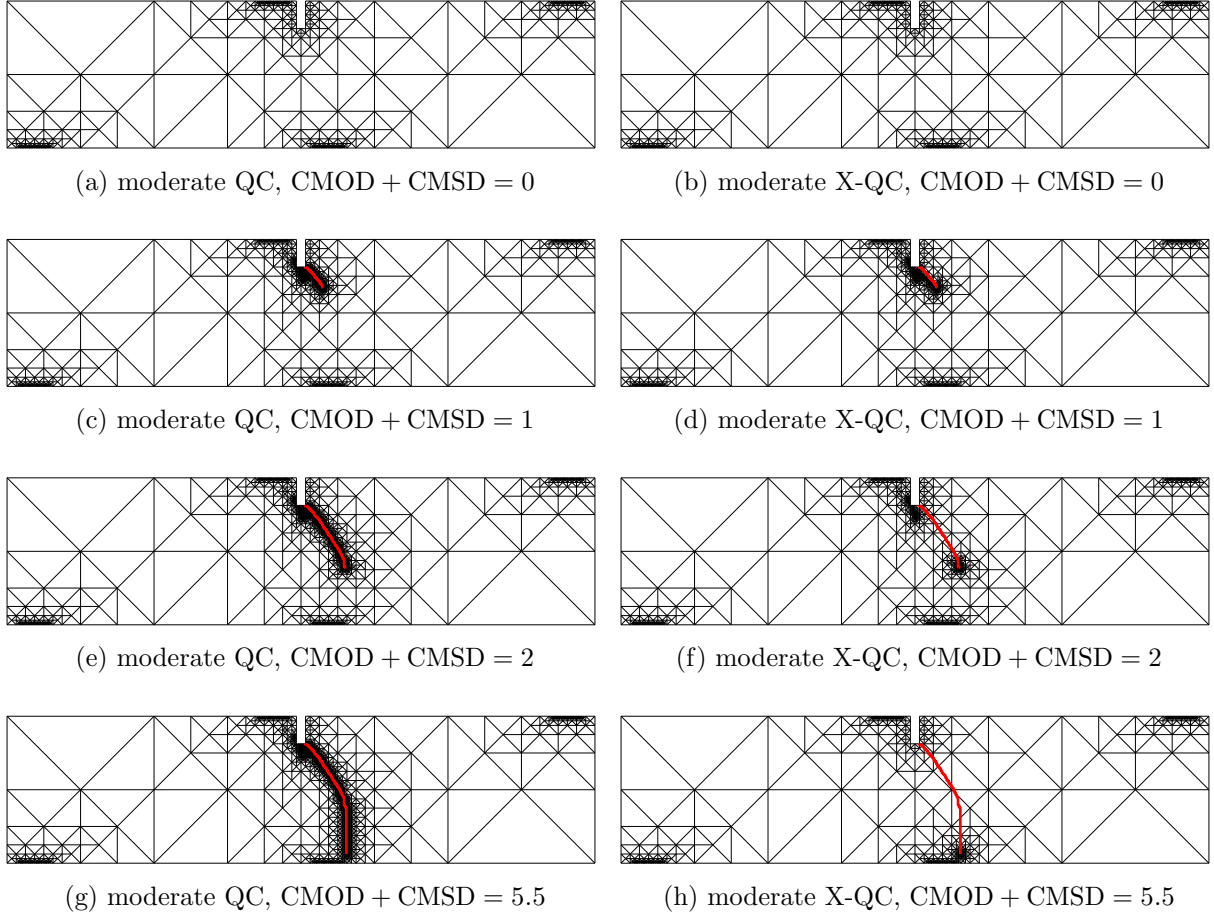
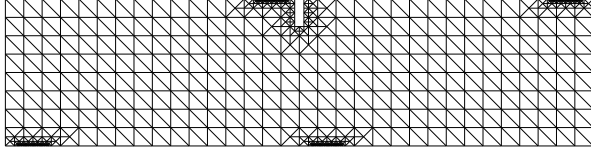
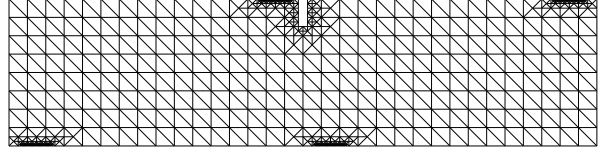


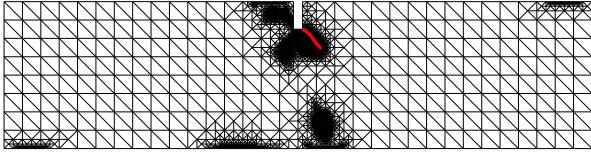
Figure 22: Eight triangulations for four-point bending test: (a), (c), (e), (g) correspond to the moderate adaptive QC approach, and (b), (d), (f), (h) to the moderate X-QC approach. The red line indicates the crack. The relative numbers of repatoms and sampling atoms are shown in Fig. 21.



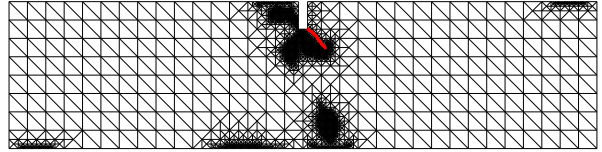
(a) progressive QC, $\text{CMOD} + \text{CMSD} = 0$



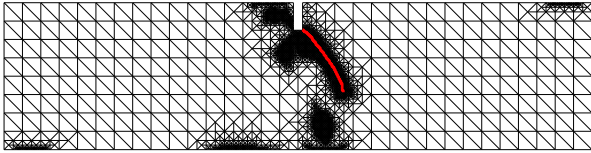
(b) progressive X-QC, $\text{CMOD} + \text{CMSD} = 0$



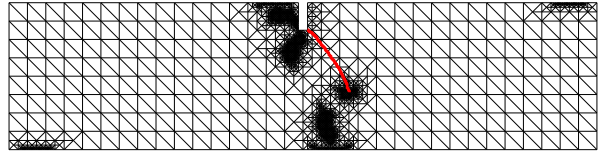
(c) progressive QC, $\text{CMOD} + \text{CMSD} = 1$



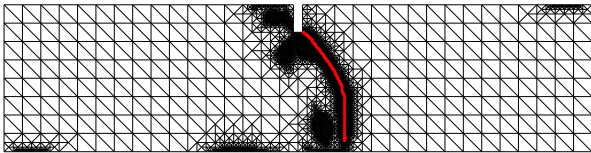
(d) progressive X-QC, $\text{CMOD} + \text{CMSD} = 1$



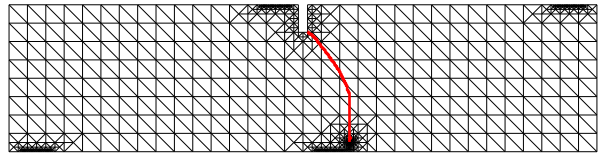
(e) progressive QC, $\text{CMOD} + \text{CMSD} = 2$



(f) progressive X-QC, $\text{CMOD} + \text{CMSD} = 2$



(g) progressive QC, $\text{CMOD} + \text{CMSD} = 5.5$



(h) progressive X-QC, $\text{CMOD} + \text{CMSD} = 5.5$

Figure 23: Eight triangulations for four-point bending test: (a), (c), (e), (g) correspond to the adaptive progressive QC approach, and (b), (d), (f), (h) to the progressive X-QC approach. The red line indicates the crack. The relative numbers of repatoms and sampling atoms are shown in Fig. 21.

6. Summary and Conclusion

In this contribution, an adaptive mesh algorithm for the variational QC for lattice networks with localized damage is developed, which refines the mesh where necessary, but also coarsens it where possible. To achieve the latter, XFEM-like enrichment functions are required. It is shown that the efficiency of the QC framework applied to lattices with localised damage increases significantly. The main results can be summarized as follows:

1. The two QC steps, interpolation and summation, were generalized to incorporate special enrichment functions, reflecting cracks within the framework of the fully-nonlocal variational QC.
2. To determine regions to be coarsened, a heuristic marking strategy was proposed with a variable parameter controlling the mesh coarseness.
3. The mesh refinement and coarsening were discussed from an energetic point of view.
4. For the investigated examples the extended QC methodology, including coarsening, reduces the number of repatoms and sampling atoms with at least 50 % of that of a simpler adaptive QC method with refinement only. The accuracy remains the same, however.

One can note that the employed coarsening procedure neglected the diffusive dissipation. This was justified for the application to localized damage, but if more ductile behaviour is modelled (due to elastic-plastic models with damage), this must be incorporated. Therefore, a further generalization is required. Moreover, instead of the heuristic marking strategies used here, goal-oriented error estimators may be used to further improve the accuracy and efficiency of the QC methodology. The variational foundation of the method provides an ideal platform for this, cf. e.g. [Radovitzky and Ortiz \(1999\)](#). The same X-QC framework can also be employed for the description of heterogeneities in otherwise homogeneous lattice networks. These aspects are, however, outside the scope of this contribution and will be reported separately.

Acknowledgements

This work was supported by the Czech Science Foundation (GAČR), through project No. 14-00420S.

References

Agathos, K., Chatzi, E., Bordas, S.P., 2016a. Stable 3D extended finite elements with higher order enrichment for accurate non planar fracture. *Computer Methods in Applied Mechanics and Engineering* 306, 19 – 46. URL: <http://www.sciencedirect.com/science/article/pii/S0045782516301050>, doi: <http://dx.doi.org/10.1016/j.cma.2016.03.023>.

- Agathos, K., Chatzi, E., Bordas, S.P.A., Talaslidis, D., 2016b. A well-conditioned and optimally convergent XFEM for 3D linear elastic fracture. *International Journal for Numerical Methods in Engineering* 105, 643–677. URL: <http://dx.doi.org/10.1002/nme.4982>, doi: 10.1002/nme.4982. nme.4982.
- Amelang, J.S., Venturini, G.N., Kochmann, D.M., 2015. Summation rules for a fully nonlocal energy-based quasicontinuum method. *Journal of the Mechanics and Physics of Solids* 82, 378–413. URL: <http://www.sciencedirect.com/science/article/pii/S0022509615000630>, doi: <http://dx.doi.org/10.1016/j.jmps.2015.03.007>.
- Aubertin, P., Réthoré, J., de Borst, R., 2009. Energy conservation of atomistic/continuum coupling. *International Journal for Numerical Methods in Engineering* 78, 1365–1386. URL: <http://dx.doi.org/10.1002/nme.2542>, doi: 10.1002/nme.2542.
- Aubertin, P., Réthoré, J., de Borst, R., 2010. A coupled molecular dynamics and extended finite element method for dynamic crack propagation. *International Journal for Numerical Methods in Engineering* 81, 72–88. URL: <http://dx.doi.org/10.1002/nme.2675>, doi: 10.1002/nme.2675.
- Babuška, I., Banerjee, U., 2012. Stable generalized finite element method (SGFEM). *Computer Methods in Applied Mechanics and Engineering* 201204, 91 – 111. URL: <http://www.sciencedirect.com/science/article/pii/S0045782511003082>, doi: <http://dx.doi.org/10.1016/j.cma.2011.09.012>.
- Babuška, I., Melenk, J.M., 1997. The partition of unity method. *International Journal for Numerical Methods in Engineering* 40, 727–758. URL: [http://dx.doi.org/10.1002/\(SICI\)1097-0207\(19970228\)40:4<727::AID-NME86>3.0.CO;2-N](http://dx.doi.org/10.1002/(SICI)1097-0207(19970228)40:4<727::AID-NME86>3.0.CO;2-N), doi: 10.1002/(SICI)1097-0207(19970228)40:4<727::AID-NME86>3.0.CO;2-N.
- Becker, R., Rannacher, R., 2001. An optimal control approach to a posteriori error estimation in finite element methods. *Acta Numerica* 10, 1–102. URL: http://journals.cambridge.org/article_S0962492901000010, doi: 10.1017/S0962492901000010.
- Beex, L.A.A., Kerfriden, P., Rabczuk, T., Bordas, S.P.A., 2014a. Quasicontinuum-based multiscale approaches for plate-like beam lattices experiencing in-plane and out-of-plane deformation. *Computer Methods in Applied Mechanics and Engineering* 279, 348–378. URL: <http://www.sciencedirect.com/science/article/pii/S0045782514002047>, doi: <http://dx.doi.org/10.1016/j.cma.2014.06.018>.
- Beex, L.A.A., Peerlings, R.H.J., Geers, M.G.D., 2011. A quasicontinuum methodology for multiscale analyses of discrete microstructural models. *International Journal for Numerical Methods in Engineering* 87, 701–718. URL: <http://dx.doi.org/10.1002/nme.3134>, doi: 10.1002/nme.3134.
- Beex, L.A.A., Peerlings, R.H.J., Geers, M.G.D., 2014b. Central summation in the quasicontinuum method. *Journal of the Mechanics and Physics of Solids* 70, 242–261. URL: <http://dx.doi.org/10.1016/j.jmps.2014.06.018>.

[//www.sciencedirect.com/science/article/pii/S0022509614001100](http://www.sciencedirect.com/science/article/pii/S0022509614001100), doi: <http://dx.doi.org/10.1016/j.jmps.2014.05.019>.

- Beex, L.A.A., Peerlings, R.H.J., Geers, M.G.D., 2014c. A multiscale quasicontinuum method for dissipative lattice models and discrete networks. *Journal of the Mechanics and Physics of Solids* 64, 154–169. URL: <http://www.sciencedirect.com/science/article/pii/S0022509613002445>, doi: <http://dx.doi.org/10.1016/j.jmps.2013.11.010>.
- Beex, L.A.A., Peerlings, R.H.J., Geers, M.G.D., 2014d. A multiscale quasicontinuum method for lattice models with bond failure and fiber sliding. *Computer Methods in Applied Mechanics and Engineering* 269, 108–122. URL: <http://www.sciencedirect.com/science/article/pii/S004578251300279X>, doi: <http://dx.doi.org/10.1016/j.cma.2013.10.027>.
- Beex, L.A.A., Peerlings, R.H.J., van Os, K., Geers, M.G.D., 2015a. The mechanical reliability of an electronic textile investigated using the virtual-power-based quasicontinuum method. *Mechanics of Materials* 80, Part A, 52–66. URL: <http://www.sciencedirect.com/science/article/pii/S0167663614001495>, doi: <http://dx.doi.org/10.1016/j.mechmat.2014.08.001>.
- Beex, L.A.A., Rokoš, O., Zeman, J., Bordas, S.P.A., 2015b. Higher-order quasicontinuum methods for elastic and dissipative lattice models: uniaxial deformation and pure bending. *GAMM-Mitteilungen* 38, 344–368. URL: <http://dx.doi.org/10.1002/gamm.201510018>, doi: [10.1002/gamm.201510018](http://dx.doi.org/10.1002/gamm.201510018).
- Beex, L.A.A., Verberne, C.W., Peerlings, R.H.J., 2013. Experimental identification of a lattice model for woven fabrics: Application to electronic textile. *Composites Part A: Applied Science and Manufacturing* 48, 82–92. URL: <http://www.sciencedirect.com/science/article/pii/S1359835X13000134>, doi: <http://dx.doi.org/10.1016/j.compositesa.2012.12.014>.
- Belytschko, T., Black, T., 1999. Elastic crack growth in finite elements with minimal remeshing. *International Journal for Numerical Methods in Engineering* 45, 601–620. URL: [http://dx.doi.org/10.1002/\(SICI\)1097-0207\(19990620\)45:5<601::AID-NME598>3.0.CO;2-S](http://dx.doi.org/10.1002/(SICI)1097-0207(19990620)45:5<601::AID-NME598>3.0.CO;2-S), doi: [10.1002/\(SICI\)1097-0207\(19990620\)45:5<601::AID-NME598>3.0.CO;2-S](http://dx.doi.org/10.1002/(SICI)1097-0207(19990620)45:5<601::AID-NME598>3.0.CO;2-S).
- Belytschko, T., Moës, N., Usui, S., Parimi, C., 2001. Arbitrary discontinuities in finite elements. *International Journal for Numerical Methods in Engineering* 50, 993–1013. URL: [http://dx.doi.org/10.1002/1097-0207\(20010210\)50:4<993::AID-NME164>3.0.CO;2-M](http://dx.doi.org/10.1002/1097-0207(20010210)50:4<993::AID-NME164>3.0.CO;2-M), doi: [10.1002/1097-0207\(20010210\)50:4<993::AID-NME164>3.0.CO;2-M](http://dx.doi.org/10.1002/1097-0207(20010210)50:4<993::AID-NME164>3.0.CO;2-M).
- Bosco, E., Peerlings, R., Geers, M., 2015a. Explaining irreversible hygroscopic strains in paper: a multi-scale modelling study on the role of fibre activation and micro-compressions. *Mechanics of Materials* 91, Part 1, 76 – 94. URL: <http://www.sciencedirect.com/science/article/pii/S0167663615000134>.

- [com/science/article/pii/S016766361500157X](http://www.sciencedirect.com/science/article/pii/S016766361500157X), doi: <http://dx.doi.org/10.1016/j.mechmat.2015.07.009>.
- Bosco, E., Peerlings, R.H., Geers, M.G., 2015b. Predicting hygro-elastic properties of paper sheets based on an idealized model of the underlying fibrous network. *International Journal of Solids and Structures* 5657, 43 – 52. URL: <http://www.sciencedirect.com/science/article/pii/S0020768314004600>, doi: <http://dx.doi.org/10.1016/j.ijsolstr.2014.12.006>.
- Bourdin, B., 2007. Numerical implementation of the variational formulation for quasi-static brittle fracture. *Interfaces and Free Boundaries* 9, 411–430. doi: [10.4171/IFB/171](https://doi.org/10.4171/IFB/171).
- Bourdin, B., Francfort, G.A., Marigo, J.J., 2000. Numerical experiments in revisited brittle fracture. *Journal of the Mechanics and Physics of Solids* 48, 797–826. URL: <http://www.sciencedirect.com/science/article/pii/S0022509699000289>, doi: [http://dx.doi.org/10.1016/S0022-5096\(99\)00028-9](http://dx.doi.org/10.1016/S0022-5096(99)00028-9).
- Bourdin, B., Francfort, G.A., Marigo, J.J., 2008. *The Variational Approach to Fracture*. Springer Netherlands. URL: <http://www.springer.com/gp/book/9781402063947>.
- Burke, S., Ortner, C., Sli, E., 2010. An Adaptive Finite Element Approximation of a Variational Model of Brittle Fracture. *SIAM Journal on Numerical Analysis* 48, 980–1012. URL: <http://epubs.siam.org/doi/abs/10.1137/080741033>, doi: [10.1137/080741033](https://doi.org/10.1137/080741033).
- Carstensen, C., Hackl, K., Mielke, A., 2002. Non-convex potentials and microstructures in finite-strain plasticity. *R. Soc. Lond. Proc. Ser. A Math. Phys. Eng. Sci.* 458, 299–317. doi: [10.1098/rspa.2001.0864](https://doi.org/10.1098/rspa.2001.0864).
- Chen, L., Zhang, C.S., 2010. A coarsening algorithm on adaptive grids by newest vertex bisection and its applications. *J. Comp. Math.* 28, 767–789.
- Curtin, W.A., Miller, R.E., 2003. Atomistic/continuum coupling in computational materials science. *Modelling and Simulation in Materials Science and Engineering* 11, R33. URL: <http://stacks.iop.org/0965-0393/11/i=3/a=201>.
- Cusatis, G., Bažant, Z.P., Cedolin, L., 2006. Confinement-shear lattice CSL model for fracture propagation in concrete. *Computer Methods in Applied Mechanics and Engineering* 195, 7154–7171. URL: <http://www.sciencedirect.com/science/article/pii/S0045782505003956>, doi: <http://dx.doi.org/10.1016/j.cma.2005.04.019>.
- Eliáš, J., Vořechovský, M., Skoček, J., Bažant, Z.P., 2015. Stochastic discrete meso-scale simulations of concrete fracture: Comparison to experimental data. *Engineering Fracture Mechanics* 135, 1–16. URL: <http://www.sciencedirect.com/science/article/pii/S0013794415000053>, doi: <http://dx.doi.org/10.1016/j.engfracmech.2015.01.004>.

- Fries, T.P., 2008. A corrected XFEM approximation without problems in blending elements. *International Journal for Numerical Methods in Engineering* 75, 503–532. URL: <http://dx.doi.org/10.1002/nme.2259>, doi: 10.1002/nme.2259.
- Fries, T.P., Baydoun, M., 2012. Crack propagation with the extended finite element method and a hybrid explicit–implicit crack description. *International Journal for Numerical Methods in Engineering* 89, 1527–1558. URL: <http://dx.doi.org/10.1002/nme.3299>, doi: 10.1002/nme.3299.
- Fries, T.P., Belytschko, T., 2010. The extended/generalized finite element method: An overview of the method and its applications. *International Journal for Numerical Methods in Engineering* 84, 253–304. URL: <http://dx.doi.org/10.1002/nme.2914>, doi: 10.1002/nme.2914.
- Funken, S., Praetorius, D., Wissgott, P., 2010. Efficient implementation of adaptive P1-FEM in Matlab. *Comput. Methods Appl. Math.* 11, 460–490. doi: 10.2478/cmam-2011-0026.
- Gracie, R., Belytschko, T., 2009. Concurrently coupled atomistic and XFEM models for dislocations and cracks. *International Journal for Numerical Methods in Engineering* 78, 354–378. URL: <http://dx.doi.org/10.1002/nme.2488>, doi: 10.1002/nme.2488.
- Grassl, P., Jirásek, M., 2010. Meso-scale approach to modelling the fracture process zone of concrete subjected to uniaxial tension. *International Journal of Solids and Structures* 47, 957–968. URL: <http://www.sciencedirect.com/science/article/pii/S0020768309004752>, doi: <http://dx.doi.org/10.1016/j.ijsolstr.2009.12.010>.
- Griebel, M., Schweitzer, M.A., 2000. A particle-partition of unity method for the solution of elliptic, parabolic, and hyperbolic PDEs. *SIAM Journal on Scientific Computing* 22, 853–890. URL: <http://dx.doi.org/10.1137/S1064827599355840>, doi: 10.1137/S1064827599355840, arXiv:<http://dx.doi.org/10.1137/S1064827599355840>.
- Han, W., Reddy, B.D., 1995. Computational plasticity: The variational basis and numerical analysis. *Computational Mechanics Advances* 2, 283–400.
- Hofacker, M., Miehe, C., 2012. Continuum phase field modeling of dynamic fracture: variational principles and staggered FE implementation. *International Journal of Fracture* 178, 113–129. URL: <http://dx.doi.org/10.1007/s10704-012-9753-8>, doi: 10.1007/s10704-012-9753-8.
- Iyer, M., Gavini, V., 2011. A field theoretical approach to the quasi-continuum method. *Journal of the Mechanics and Physics of Solids* 59, 1506–1535. URL: <http://www.sciencedirect.com/science/article/pii/S0022509610002425>, doi: <http://dx.doi.org/10.1016/j.jmps.2010.12.002>.
- Jirásek, M., Bažant, Z.P., 2002. *Inelastic Analysis of Structures*. John Wiley & Sons. URL: <https://books.google.nl/books?id=8mz-xPdvH00C>.

- Jirásek, M., Zeman, J., 2015. Localization study of a regularized variational damage model. *International Journal of Solids and Structures* 6970, 131–151. URL: <http://www.sciencedirect.com/science/article/pii/S0020768315002620>, doi: <http://dx.doi.org/10.1016/j.ijsolstr.2015.06.001>.
- Kulachenko, A., Uesaka, T., 2012. Direct simulations of fiber network deformation and failure. *Mechanics of Materials* 51, 1–14. URL: <http://www.sciencedirect.com/science/article/pii/S0167663612000683>, doi: <http://dx.doi.org/10.1016/j.mechmat.2012.03.010>.
- Laborde, P., Pommier, J., Renard, Y., Salan, M., 2005. High-order extended finite element method for cracked domains. *International Journal for Numerical Methods in Engineering* 64, 354–381. URL: <http://dx.doi.org/10.1002/nme.1370>, doi: [10.1002/nme.1370](http://dx.doi.org/10.1002/nme.1370).
- Liu, J.X., Chen, Z.T., Li, K.C., 2010. A 2-D lattice model for simulating the failure of paper. *Theoretical and Applied Fracture Mechanics* 54, 1–10. URL: <http://www.sciencedirect.com/science/article/pii/S016784421000039X>, doi: <http://dx.doi.org/10.1016/j.tafmec.2010.06.009>.
- Luskin, M., Ortner, C., 2013. Atomistic-to-continuum coupling. *Acta Numerica* 22, 397–508. URL: http://journals.cambridge.org/article_S0962492913000068, doi: [10.1017/S0962492913000068](http://dx.doi.org/10.1017/S0962492913000068).
- Melenk, J., Babuška, I., 1996. The partition of unity finite element method: Basic theory and applications. *Computer Methods in Applied Mechanics and Engineering* 139, 289 – 314. URL: <http://www.sciencedirect.com/science/article/pii/S0045782596010870>, doi: [http://dx.doi.org/10.1016/S0045-7825\(96\)01087-0](http://dx.doi.org/10.1016/S0045-7825(96)01087-0).
- Memarnahavandi, A., Larsson, F., Runesson, K., 2015. A goal-oriented adaptive procedure for the quasi-continuum method with cluster approximation. *Computational Mechanics* 55, 617–642. URL: <http://dx.doi.org/10.1007/s00466-015-1127-4>, doi: [10.1007/s00466-015-1127-4](http://dx.doi.org/10.1007/s00466-015-1127-4).
- Mesgarnejad, A., Bourdin, B., Khonsari, M.M., 2015. Validation simulations for the variational approach to fracture. *Computer Methods in Applied Mechanics and Engineering* 290, 420–437. URL: <http://www.sciencedirect.com/science/article/pii/S004578251400423X>, doi: <http://dx.doi.org/10.1016/j.cma.2014.10.052>.
- Mielke, A., 2003. Energetic formulation of multiplicative elasto-plasticity using dissipation distances. *Continuum Mechanics and Thermodynamics* 15, 351–382. URL: <http://dx.doi.org/10.1007/s00161-003-0120-x>, doi: [10.1007/s00161-003-0120-x](http://dx.doi.org/10.1007/s00161-003-0120-x).
- Mielke, A., Roubíček, T., 2015. *Rate-Independent Systems: Theory and Application*. 1 ed., Springer-Verlag New York. URL: <http://www.springer.com/us/book/9781493927050>, doi: [10.1007/978-1-4939-2706-7](http://dx.doi.org/10.1007/978-1-4939-2706-7).

- Mielke, A., Theil, F., Levitas, V.I., 2002. A variational formulation of rate-independent phase transformations using an extremum principle. *Archive for Rational Mechanics and Analysis* 162, 137–177. URL: <http://dx.doi.org/10.1007/s002050200194>, doi: 10.1007/s002050200194.
- Miller, R.E., Tadmor, E.B., 2002. The quasicontinuum method: Overview, applications and current directions. *Journal of Computer-Aided Materials Design* 9, 203–239. URL: <http://dx.doi.org/10.1023/A:1026098010127>, doi: 10.1023/A:1026098010127.
- Miller, R.E., Tadmor, E.B., 2009. A unified framework and performance benchmark of fourteen multiscale atomistic/continuum coupling methods. *Modelling and Simulation in Materials Science and Engineering* 17, 053001. URL: <http://stacks.iop.org/0965-0393/17/i=5/a=053001>.
- Moës, N., Dolbow, J., Belytschko, T., 1999. A finite element method for crack growth without remeshing. *International Journal for Numerical Methods in Engineering* 46, 131–150. URL: [http://dx.doi.org/10.1002/\(SICI\)1097-0207\(19990910\)46:1<131::AID-NME726>3.0.CO;2-J](http://dx.doi.org/10.1002/(SICI)1097-0207(19990910)46:1<131::AID-NME726>3.0.CO;2-J), doi: 10.1002/(SICI)1097-0207(19990910)46:1<131::AID-NME726>3.0.CO;2-J.
- Mühlhaus, H.B., Aifantis, E.C., 1991. A variational principle for gradient plasticity. *International Journal of Solids and Structures* 28, 845–857. URL: <http://www.sciencedirect.com/science/article/pii/002076839190004Y>, doi: [http://dx.doi.org/10.1016/0020-7683\(91\)90004-Y](http://dx.doi.org/10.1016/0020-7683(91)90004-Y).
- Oden, J., Prudhomme, S., 2002. Estimation of modeling error in computational mechanics. *Journal of Computational Physics* 182, 496–515. URL: <http://www.sciencedirect.com/science/article/pii/S0021999102971834>, doi: <http://dx.doi.org/10.1006/jcph.2002.7183>.
- Peng, X., Cao, J., 2005. A continuum mechanics-based non-orthogonal constitutive model for woven composite fabrics. *Composites Part A: Applied Science and Manufacturing* 36, 859 – 874. URL: <http://www.sciencedirect.com/science/article/pii/S1359835X04002593>, doi: <http://dx.doi.org/10.1016/j.compositesa.2004.08.008>.
- Pham, K., Marigo, J.J., Maurini, C., 2011. The issues of the uniqueness and the stability of the homogeneous response in uniaxial tests with gradient damage models. *Journal of the Mechanics and Physics of Solids* 59, 1163–1190. URL: <http://www.sciencedirect.com/science/article/pii/S002250961100055X>, doi: <http://dx.doi.org/10.1016/j.jmps.2011.03.010>.
- Prudhomme, S., Bauman, P.T., Oden, J.T., 2006. Error control for molecular statics problems. *International Journal for Multiscale Computational Engineering* 4, 647–662. doi: 10.1615/IntJMultCompEng.v4.i5-6.60.

- Radovitzky, R., Ortiz, M., 1999. Error estimation and adaptive meshing in strongly nonlinear dynamic problems. *Computer Methods in Applied Mechanics and Engineering* 172, 203 – 240. URL: <http://www.sciencedirect.com/science/article/pii/S0045782598002308>, doi: [http://dx.doi.org/10.1016/S0045-7825\(98\)00230-8](http://dx.doi.org/10.1016/S0045-7825(98)00230-8).
- Ridruejo, A., González, C., LLorca, J., 2010. Damage micromechanisms and notch sensitivity of glass-fiber non-woven felts: An experimental and numerical study. *Journal of the Mechanics and Physics of Solids* 58, 1628–1645. URL: <http://www.sciencedirect.com/science/article/pii/S0022509610001341>, doi: <http://dx.doi.org/10.1016/j.jmps.2010.07.005>.
- Rivara, M.C., 1997. New longest-edge algorithms for the refinement and/or improvement of unstructured triangulations. *International Journal for Numerical Methods in Engineering* 40, 3313–3324. doi: [10.1002/\(SICI\)1097-0207\(19970930\)40:18<3313::AID-NME214>3.0.CO;2-#](https://doi.org/10.1002/(SICI)1097-0207(19970930)40:18<3313::AID-NME214>3.0.CO;2-#).
- Rokoš, O., Beex, L.A.A., Zeman, J., Peerlings, R.H.J., 2016a. A Variational Formulation of Dissipative Quasicontinuum Methods. ArXiv e-prints [arXiv:1601.00625](https://arxiv.org/abs/1601.00625).
- Rokoš, O., Peerlings, R.H.J., Zeman, J., Beex, L.A.A., 2016b. An Adaptive Variational Quasicontinuum Methodology for Lattice Networks with Localized Damage. ArXiv e-prints [arXiv:1601.00625](https://arxiv.org/abs/1601.00625).
- Schlangen, E., 1993. Experimental and Numerical Analysis of Fracture Processes in Concrete. Ph.D. thesis. Technische Universiteit Delft. TU Delft, 2600 AA Delft, The Netherlands.
- Schlangen, E., van Mier, J.G.M., 1992. Experimental and numerical analysis of micromechanisms of fracture of cement-based composites. *Cement and Concrete Composites* 14, 105–118. URL: <http://www.sciencedirect.com/science/article/pii/095894659290004F>, doi: [http://dx.doi.org/10.1016/0958-9465\(92\)90004-F](http://dx.doi.org/10.1016/0958-9465(92)90004-F).
- Shenoy, V.B., Miller, R., Tadmor, E.B., Rodney, D., Phillips, R., Ortiz, M., 1999. An adaptive finite element approach to atomic-scale mechanics – the quasicontinuum method. *Journal of the Mechanics and Physics of Solids* 47, 611–642. URL: <http://www.sciencedirect.com/science/article/pii/S0022509698000519>, doi: [http://dx.doi.org/10.1016/S0022-5096\(98\)00051-9](http://dx.doi.org/10.1016/S0022-5096(98)00051-9).
- Strouboulis, T., Babuška, I., Copps, K., 2000a. The design and analysis of the generalized finite element method. *Computer Methods in Applied Mechanics and Engineering* 181, 43 – 69. URL: <http://www.sciencedirect.com/science/article/pii/S0045782599000729>, doi: [http://dx.doi.org/10.1016/S0045-7825\(99\)00072-9](http://dx.doi.org/10.1016/S0045-7825(99)00072-9).
- Strouboulis, T., Copps, K., Babuška, I., 2000b. The generalized finite element method: an example of its implementation and illustration of its performance. *International Journal for Numerical Methods in Engineering* 47, 1401–1417. URL: [http://dx.doi.org/10.1016/S0022-5096\(99\)00072-9](http://dx.doi.org/10.1016/S0022-5096(99)00072-9).

[org/10.1002/\(SICI\)1097-0207\(20000320\)47:8<1401::AID-NME835>3.0.CO;2-8](https://doi.org/10.1002/(SICI)1097-0207(20000320)47:8<1401::AID-NME835>3.0.CO;2-8), doi: 10.1002/(SICI)1097-0207(20000320)47:8<1401::AID-NME835>3.0.CO;2-8.

Tadmor, E.B., Miller, R.E., 2011. Modeling Materials: Continuum, Atomistic and Multiscale Techniques. Cambridge University Press. URL: <http://books.google.cz/books?id=5PLvc6tdsjcC>.

Tadmor, E.B., Ortiz, M., Phillips, R., 1996. Quasicontinuum analysis of defects in solids. Philosophical Magazine A 73, 1529–1563. URL: <http://dx.doi.org/10.1080/01418619608243000>, doi: 10.1080/01418619608243000, arXiv:<http://dx.doi.org/10.1080/01418619608243000>.

Talebi, H., Silani, M., Bordas, S., Kerfriden, P., Rabczuk, T., 2013. Molecular dynamics/XFEM coupling by a three-dimensional extended bridging domain with applications to dynamic brittle fracture. International Journal for Multiscale Computational Engineering 11, 527–541. doi: 10.1615/IntJMultCompEng.2013005838.

Ventura, G., Gracie, R., Belytschko, T., 2009. Fast integration and weight function blending in the extended finite element method. International Journal for Numerical Methods in Engineering 77, 1–29. URL: <http://dx.doi.org/10.1002/nme.2387>, doi: 10.1002/nme.2387.

Wells, G.N., Sluys, L.J., 2001. A new method for modelling cohesive cracks using finite elements. International Journal for Numerical Methods in Engineering 50, 2667–2682. URL: <http://dx.doi.org/10.1002/nme.143>, doi: 10.1002/nme.143.

Yang, Q., To, A.C., 2015. Multiresolution molecular mechanics: A unified and consistent framework for general finite element shape functions. Computer Methods in Applied Mechanics and Engineering 283, 384–418. URL: <http://www.sciencedirect.com/science/article/pii/S0045782514003545>, doi: <http://dx.doi.org/10.1016/j.cma.2014.09.031>.